IEEE Access
Multidisciplinary ⋮ Rapid Review ⋮ Open Access Journal

Received 7 September 2025, accepted 25 December 2025, date of publication 5 January 2026, date of current version 8 January 2026.

Digital Object Identifier 10.1109/ACCESS.2025.3650505

RESEARCH ARTICLE

Azimuth DOA Estimation Using Concentric Coprime Uniform Circular Array With Sparse Bayesian Learning

SANJAY PANDAV[1,2] AND P. UBAIDULLA[3], (Senior Member, IEEE)
[1]DLRL, DRDO, Hyderabad 500005, India
[2]SPCRC, IIIT Hyderabad 500032, India
[3]Independent Researcher, Hyderabad 500019, India

Corresponding author: Sanjay Pandav (sanjaypandav@gmail.com)

ABSTRACT Estimation of direction-of-arrival (DOA) is a fundamental problem in array signal processing. The uniform circular array (UCA) is a highly useful array geometry for DOA estimation, especially in electronic warfare (EW), as it possesses useful properties such as complete 360° azimuth coverage and DOA estimation accuracy that is almost invariant with azimuth unlike linear array (LA). In addition, it is well suited for physical installation on complex platforms such as aircraft, ship, and autonomous aerial vehicle (AAV). Given the inherent sparsity of the DOA parameter in the azimuth domain, the last decade has seen significant research applying compressed sensing and sparse signal recovery with sparse array geometries. The difference co-array of virtual sensors of the physical array is dense; hence, sparse arrays can provide more accurate DOA estimation. In this paper, we propose a novel sparse array geometry called a concentric coprime uniform circular array (CCUCA) and perform azimuth DOA estimation by employing sparse Bayesian learning (SBL) with the difference co-array. This antenna array geometry is well suited for installation on complex platforms used for surveillance in EW compared to a nested sparse circular array (NSCA). The results of numerical experiments demonstrate the performance of the proposed technique. We also present the design of a novel passive frequency-independent CCUCA simulator, which can be realized using radio-frequency (RF) power dividers and delay lines. This can be used for generating multiple RF signals with appropriate phases for laboratory testing of the DOA estimation system realized using phase-coherent, multichannel RF and digital signal processing (DSP) hardware.

INDEX TERMS Direction-of-arrival (DOA) estimation, electronic warfare (EW), signal intelligence (SIGINT), sparse antenna arrays, sparse Bayesian learning (SBL), uniform circular array (UCA).

I. INTRODUCTION

Estimation of direction-of-arrival (DOA) is a fundamental problem in array signal processing that has been studied for more than a century [1], [2], [3], [4], [5]. The uniform circular array (UCA) is an extremely useful geometry for DOA estimation in applications like spectrum monitoring (SM) and signal intelligence (SIGINT) operations in electronic warfare (EW), as it possesses useful properties such as complete 360° azimuth coverage, DOA estimation accuracy that is almost invariant with azimuth unlike linear array (LA), and ease of physical installation on complex platforms like aircraft, ship, autonomous aerial vehicle (AAV), etc. It is well known that the accuracy of DOA estimation is heavily dependent on the aperture size of the antenna array of any geometry, including the UCA. For a fixed number of antenna elements in the UCA, the radius of the physical array cannot be arbitrarily increased to improve the DOA accuracy due to a violation of the spatial Nyquist sampling theorem. Given the inherent sparsity of the DOA parameter in the azimuth domain, extensive research has been conducted over the past and present decades to explore the application of techniques such as compressed sensing and sparse signal recovery [6], [7], [8], [9], [10], [11]. These techniques have been shown

The associate editor coordinating the review of this manuscript and approving it for publication was Manuel Rosa-Zurera.

to improve the accuracy of DOA estimation using the sparse array geometries [12], [13], [14], [15], [16], [17]. Unlike conventional subspace-based DOA estimation algorithms such as multiple signal classification (MUSIC) [18], and estimation of signal parameters via rotational invariance technique (ESPRIT) [19], the sparse signal recovery techniques can handle scenarios with correlated sources or emitters [6], [20], [21]. They also handle underdetermined cases where the number of sources exceeds the number of antennas/ sensors.

It is worth noting that in the 1960s, extensive research [22] was carried out on unequally spaced, as well as thinned arrays to increase the aperture of the array without increasing the number of antenna elements. The important concept of the difference co-array of virtual sensors of the physical array was introduced in [23]. The difference co-array of several sparse arrays of sensors, like minimum redundancy array [24], nested array [12], coprime array [13], [25], [26], [27], [28] *etc.*, is dense in comparison to their corresponding physical arrays. This results in enhanced degrees of freedom, and hence sparse arrays can provide more accurate DOA estimation, although they usually require more computations than traditional subspace approaches [29].

The majority of the reported work studies linear geometries for sparse arrays. In this context, a generalized coprime array was introduced in [14], and the concept of a super-nested array was presented in [15]. DOA estimation with linear arrays using sparse Bayesian learning (SBL) [9], [10], [30] has been reported in [31], [32], [33], and [34]. However, one major drawback of linear arrays is that achieving 360° azimuth coverage on complex platforms requires the installation of multiple linear arrays. This is due to the interference caused by platform-supporting structures and the resulting obstructions they create. Each linear array would then provide coverage of a certain azimuth sector. However, in such scenarios, the complexity of the hardware varies depending on whether each of the arrays has its own dedicated phase-coherent RF chain or whether they share one [35]. A trade-off between the probability of intercept and constraints on size, weight, power consumption, etc., drives this design choice. The analysis of a 'V'-shaped sparse array for 2-D direction-of-arrival (DOA) estimation is detailed in [36]. Meanwhile, 2-D DOA estimation utilizing an 'L'-shaped sparse array is described in [37]. In [17], design of a non-integer array, which is constrained by both the number of sensors and the aperture, for 1-D DOA estimation is presented. Furthermore, the performance of azimuth DOA estimation in various geometric configurations was evaluated using MUSIC in [17]. Estimation of 2-D off-grid DOA using a uniform plane array (UPA) based on structured SBL was presented in [38].

DOA estimation with a ULA utilizing multiple convolutional neural networks (CNNs), was recently proposed as DeepMUSIC [39]. DOA estimation in the low signal-to-noise power ratio (SNR) regime using a denoising autoencoder model [40] and CNN-based approach [41] with ULA setups has been studied. An improved DOA estimation algorithm based on an optimal deep residual neural network classifier for ULA is described [42]. Recently, deep learning (DL) models based on attention mechanisms for DOA estimation have been reported to perform well in low SNR scenarios [43], [44], [45]. However, these models require an extensive, diverse, and realistic training dataset and are often difficult to interpret compared to those based on sparse recovery-based approaches such as SBL.

DOA estimation approaches based on subspace techniques like MUSIC [25], [26], [27] and ESPRIT can only utilize the lags associated with the contiguous portion of the difference co-array when used with sparse LA. This is due to the constraint on the steering vector, also known as the beam steering vector or the manifold vector, to have a Vandermonde structure. However, all the lags in the difference co-arrays can be utilized for sparse recovery when the ℓ_1 optimization approach is used instead of subspace-based techniques. It is important to mention that in the uniform circular array (UCA), the steering vector lacks the typical Vandermonde structure seen in the element space in the case of uniform linear arrays (ULAs) [2], [3], [16], [46]. Estimation of DOA using the ℓ_1 optimizer with nested sparse circular array (NSCA) and a sparse super-nested circular array has been studied recently [47], [48], [49]. The results reported on the NSCA in [47] assume that the radius of the NSCA is equal to one wavelength. The NSCA geometry requires an antenna to be located in the center of the array. This could be a limitation for platform installation due to typical constraints encountered in practice, *viz.*, presence of other platform sensors at that location, presence of other platform structures which cannot be relocated, presence of central structural mast on certain platforms that do not permit locating an antenna, *etc.* In the NSCA [48], there are two circular sub-arrays. The first circular sub-array is dense compared to the other. The dense sub-array elements could result in considerable mutual coupling that is a function of the frequency as well as the azimuth. This mutual coupling will degrade the DOA estimation performance unless it is accounted for. Another limitation that could arise when operating at higher frequencies is that it may be infeasible to position the dense sub-array due to the physical size of the antenna elements. One way to overcome this limitation is to increase the radius of the NSCA beyond one wavelength. This also improves the accuracy of the DOA estimation and is established in this paper through numerical simulations. Since the NSCA geometry is not symmetric in azimuth [48], it can pose problems for installation on platforms such as AAV and aircraft with respect to the endurance and center of gravity of the platform.

In this paper, we introduce the design of a new array geometry to address the aforementioned challenges and propose a azimuth DOA estimation algorithm that uses the SBL on the data received by the corresponding difference

co-array. The proposed approach complements the referred DL-based methods by exploiting the difference co-array structure and has the important advantage of not requiring a realistic and diverse training dataset, which is difficult to provide in EW scenarios. The main contributions of this paper can be summarized as follows.

i. We propose a novel array configuration, termed the concentric coprime uniform circular array (CCUCA), and analyze the structure of its difference co-array. This configuration comprises of two concentric UCAs. Unlike the NSCA, this design does not require the placement of an antenna element at the center of the array. The proposed geometry is more suitable for installation on platforms like a ship, AAV, or aircraft, keeping in view constraints like platform endurance, center of gravity, mutual coupling of dense sub-arrays, and reduced feasibility of locating physically large antennas in the dense sub-array when operating at higher frequencies. An added advantage of this array is that it is based on the UCA geometry, for which the DOA accuracy is almost independent of the azimuth because of its inherent symmetry in the azimuth.
ii. We propose an SBL-based DOA estimation algorithm that uses the difference co-array of both CCUCA and NSCA with the capability to handle more number of sources than the physical sensors in the array. The SBL algorithm is found to promote sparsity in large-dimensional problems and possesses faster convergence compared to the ℓ_1 optimizer such as matching pursuit (MP) [50]. The results of numerical experiments are presented to validate the proposed approach. The numerical experiments also demonstrate that the DOA estimation accuracy of the NSCA using the SBL is improved by increasing the array radius as well as the number of antennas.
iii. We present the design of a novel passive frequency-independent CCUCA simulator. The simulator is valuable for testing the algorithms on the target hardware in the laboratory. This is achieved by injecting RF signals with phases that accurately represent the delays experienced in receiving the signals at the individual antennas of the array. This approach of testing avoids the frequent field measurement campaigns that are time-consuming, cumbersome, and expensive. The proposed approach can be easily adapted to design a passive frequency-independent antenna array simulator for antenna arrays that have arbitrary geometry.

The rest of the paper is structured as follows. Section II presents the geometry of the proposed CCUCA and the mathematical signal model of the corresponding difference co-array. Section III presents how the difference co-array data are exploited to estimate the DOA of sources using SBL. Performance analysis and results obtained through numerical experiments for the CCUCA and the NSCA are presented in Section IV. Section V presents the design of a novel passive frequency-independent CCUCA simulator. Finally, Section VI concludes the paper.

Notations: Matrices and vectors are denoted in boldface uppercase and lowercase letters, respectively. $\emptyset$, $\{e\}$, and $\cup$ denote an empty set, a singleton set with an element e, and the union operator for sets, respectively. j, $(\cdot)^*$, $(\cdot)^T$, $(\cdot)^H$, $\mathbb{R}^N$, $\mathbb{C}^N$, $\mathbf{0}$ and $\mathbf{I}_N$ stand for $\sqrt{-1}$, complex conjugate, transpose, complex conjugate transpose, N-dimensional real vector space, N-dimensional complex vector space, zero matrix of appropriate dimensions and $N \times N$ identity matrix, respectively. $\delta(\cdot)$, $f(\cdot)$, $\exp(\cdot)$, $\log(\cdot)$, $\mathbb{E}(\cdot)$, $\otimes$, $vec(\cdot)$, $\text{diag}(\mathbf{x})$, and $\text{angle}(\cdot)$ denote the Dirac delta function, probability density function, exponential function, natural logarithm function, statistical expectation operator, Kronecker product, vectorization operator that transforms a matrix into a vector by stacking all columns vertically, diagonal matrix that uses elements of $\mathbf{x}$ as diagonal elements, and phase angle operator for a complex number, respectively. The operator $|\cdot|$ denotes the cardinality of a set, the absolute value of the complex number, and the replacement of the elements of a complex vector with their corresponding absolute values, depending on the context. For a vector $\mathbf{z} \in \mathbb{C}^N$, $\{\mathbf{z}\}$ and $|\{\mathbf{z}\}|$ denote the set constructed with the elements of vector $\mathbf{z}$ and the length of the vector, *i.e.* N, respectively. $\mathfrak{Re}(\cdot)$ denotes the real part of a complex number and the operation of replacing the elements of a complex vector with their corresponding real parts, depending on the context. For any real number $p \geq 1$, $\|\cdot\|_p$ denotes the ℓ_p norm of the input vector. $\mathbf{\Sigma}(m_1 : n_1,\ m_2 : n_2)$ is the sub-matrix constructed using rows, m_1 to n_1 and columns, m_2 to n_2 of matrix $\mathbf{\Sigma}$. The sub-matrix of $\mathbf{\Sigma}$ constructed using columns m_2 to n_2 is denoted as $\mathbf{\Sigma}(:,\ m_2 : n_2)$. Similarly, if the set R_C denotes the index set of columns that have been sorted according to a defined criterion, then $\mathbf{\Sigma}(:,\ R_C)$, denotes the sub-matrix of $\mathbf{\Sigma}$ constructed using the column indices in the set R_C. $Tr\{\cdot\}$ denotes the trace of the square matrix. $\mathbf{z} \sim \mathcal{CN}(\boldsymbol{\mu}_z, \mathbf{\Sigma}_z)$ denotes that random vector $\mathbf{z}$ has a circularly symmetric Gaussian distribution with mean vector $\boldsymbol{\mu}_z$ and covariance matrix $\mathbf{\Sigma}_z$. The dot product between two vectors $\mathbf{x}$ and $\mathbf{y}$ of appropriate dimensions is denoted by $\mathbf{x}.\mathbf{y}$. $\min(M, N)$, and $\max(M, N)$, denote, respectively, the minimum and maximum of natural numbers M and N. $\gcd(M, N)$ denotes the greatest common divider of natural numbers M and N. $a \bmod (b)$ denotes the modulo operation that provides the remainder of the Euclidean division of integer a by integer b, where a is the dividend and b is the divisor.

II. CONCENTRIC COPRIME UNIFORM CIRCULAR ARRAY AND THE MATHEMATICAL SIGNAL MODEL OF ITS DIFFERENCE CO-ARRAY

A. CONCENTRIC COPRIME UNIFORM CIRCULAR ARRAY

Figure 1 shows the geometry of the proposed CCUCA. It consists of two concentric uniform circular arrays in the X-Y plane with radius R_1 and R_2, respectively. We refer to these arrays as UCA 1 and UCA 2, respectively. UCA 1 has

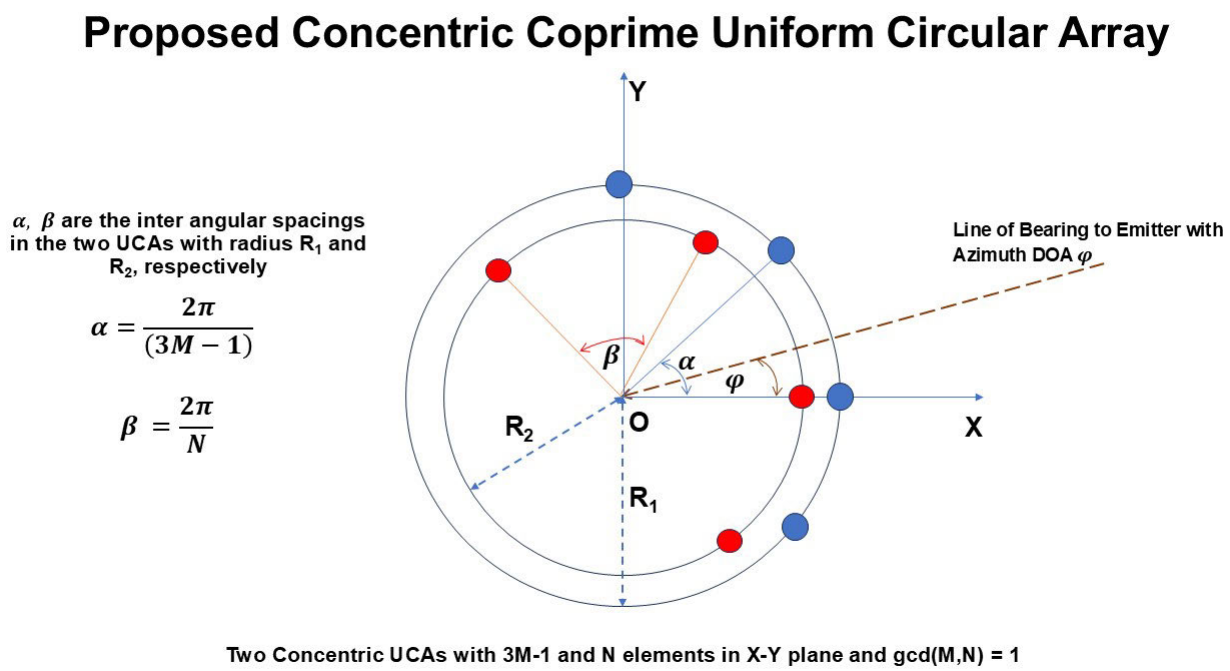

FIGURE 1. Geometry of the proposed CCUCA.

$3M-1$ antennas, and UCA 2 has N antennas with M and N being coprime natural numbers, *i.e.* $\gcd(M,N)=1$.

An additional condition that must be imposed is that if $R_1 = R_2$, then $3M-1 \neq N$ to ensure that the physical locations of the UCA 1 and UCA 2 sensors are distinct for all sensors except one. Thus, the total number of physical antennas in the CCUCA is $3M+N-1$. The angular inter-element spacing between the physical sensors in UCA 1 is given by

$$\alpha = \frac{2\pi}{3M-1}, \tag{1}$$

and that in UCA 2 is given by

$$\beta = \frac{2\pi}{N}. \tag{2}$$

The antennas of the CCUCA are assumed to be identical with isotropic radiation patterns. The far-field source/emitter is assumed to be in the same plane as the CCUCA. A narrowband electromagnetic (EM) plane wave of wavelength λ radiated by the source is received from an azimuth DOA φ. The array is considered sparse when R_1 and R_2 are greater than λ. This array is a UCA version of the modified parallel coprime linear sub-arrays proposed in [51], where both sub-arrays were oriented parallel to the X-axis. The first sub-array was located along the X-axis, whereas the second sub-array was displaced from the first by a distance $d \leq \frac{\lambda}{2}$ measured along the Y direction. Sparsity in CCUCA results in less mutual coupling in contrast to conventional non-sparse UCA. An added advantage of CCUCA is its larger aperture, both for the physical array and its difference co-array [§]. Let $\mathrm{S}_1 \overset{\text{def}}{=} \{1-M, 2-M, 3-M, \ldots, 0, \ldots, 2M-1\}$, $\mathrm{S}_1' \overset{\text{def}}{=} \{1, 2, 3, \ldots, 3M-1\}$, $\mathrm{S}_2 \overset{\text{def}}{=} \{0, 1, \ldots, N-1\}$, $\mathrm{S}_2'' \overset{\text{def}}{=} \{1, 2, \ldots, N\}$, and $\mathrm{S} \overset{\text{def}}{=} \{1, 2, 3, \ldots, 3M-1, 3M, 3M+1, \ldots, (3M-1)N\}$. We can then express the position vector of the m^{th} antenna element of UCA 1 as

$$\mathbf{p}_m' = x_m'\hat{\mathbf{x}} + y_m'\hat{\mathbf{y}},\ m \in \mathrm{S}_1', \tag{3}$$

where (x_m', y_m') are the Cartesian coordinates of the m^{th} antenna element of UCA 1 given by

$$\left(x_m', y_m'\right) = \left(R_1 \cos\left\{\nu_m'\right\}, R_1 \sin\left\{\nu_m'\right\}\right),\ m \in \mathrm{S}_1', \tag{4}$$

with,

$$\nu_m' \overset{\text{def}}{=} (m-M)\,\alpha,\ m \in \mathrm{S}_1'. \tag{5}$$

Similarly, we can express the position vector of the n^{th} antenna element of UCA 2 as

$$\mathbf{p}_n'' = x_n''\hat{\mathbf{x}} + y_n''\hat{\mathbf{y}},\ n \in \mathrm{S}_2'', \tag{6}$$

where (x_n'', y_n'') are the Cartesian coordinates of the n^{th} antenna element of UCA 2 given by

$$\left(x_n'', y_n''\right) = \left(R_2 \cos\left\{\nu_n''\right\}, R_2 \sin\left\{\nu_n''\right\}\right),\ n \in \mathrm{S}_2'', \tag{7}$$

with,

$$\nu_n'' \overset{\text{def}}{=} (n-1)\,\beta,\ n \in \mathrm{S}_2''. \tag{8}$$

[§]Larger aperture justifies the assumption of ignoring the mutual coupling among antennas.

The wave vector $\hat{\mathbf{k}}$ in the azimuthal direction φ can be expressed as

$$\hat{\mathbf{k}} = -\frac{2\pi}{\lambda}\left(\cos[\varphi]\,\hat{\mathbf{x}} + \sin[\varphi]\,\hat{\mathbf{y}}\right), \tag{9}$$

where $\hat{\mathbf{x}}$ and $\hat{\mathbf{y}}$ represent the unit vectors in the X and Y directions, respectively. The negative sign indicates that the wave propagates towards the receiving antenna array. The steering vectors of UCA 1 and UCA 2 in direction φ are denoted by the column vectors $\boldsymbol{a}_1(\varphi) \in \mathbb{C}^{3M-1}$ and $\boldsymbol{a}_2(\varphi) \in \mathbb{C}^N$, respectively [‡‡]. The m^{th} element of $\boldsymbol{a}_1(\varphi)$ is given by

$$a'_m(\varphi) = \exp\left\{ j\psi'_m(\varphi)\right\} \quad m \in \mathrm{S}'_1, \tag{10}$$

where

$$\psi'_m(\varphi) = \left(-\hat{\mathbf{k}}\right)\cdot \mathbf{p}'_m \tag{11}$$

$$= \frac{2\pi R_1}{\lambda}\cos\left(\nu'_m - \varphi\right), \; m \in \mathrm{S}'_1. \tag{12}$$

The n^{th} element of $\boldsymbol{a}_2(\varphi)$ is given by

$$a''_n(\varphi) = \exp\left\{ j\psi''_n(\varphi)\right\} \quad n \in \mathrm{S}''_2, \tag{13}$$

where

$$\psi''_n(\varphi) = \left(-\hat{\mathbf{k}}\right)\cdot \mathbf{p}''_n \tag{14}$$

$$= \frac{2\pi R_2}{\lambda}\cos\left(\nu''_n - \varphi\right), \; n \in \mathrm{S}''_2. \tag{15}$$

The quantities ψ'_m and ψ''_n, in (11) and (14), respectively, represent the phase of the signals received [4] by the m^{th} antenna of UCA 1 and the n^{th} antenna of UCA 2. The center of the CCUCA is the phase center of the array, and we arbitrarily assign zero phase for this reference without loss of generality. The time delay in the far-field narrowband signal to propagate to the individual antennas of the CCUCA with respect to the phase center manifests itself in the form of a phase delay at the carrier frequency $\frac{C}{\lambda}$, where C, being the speed of the EM wave in free space, *i.e.*, 3×10^8 ms^{-1}.

B. DIFFERENCE CO-ARRAY OF THE CCUCA

The use of a compressed sensing signal processing framework to estimate parameters such as DOA from the undersampled measurements obtained from CCUCA leverages the virtual difference co-array structure [16]. The steering vector $\boldsymbol{a}(\varphi) \in \mathbb{C}^{(3M-1)N}$ of the difference co-array of CCUCA is obtained using the Kronecker product of the steering vectors of UCA 1 and UCA 2 as follows.

$$\mathbf{a}(\varphi) = \mathbf{a}_1(\varphi) \otimes \mathbf{a}_2^*(\varphi). \tag{16}$$

The l^{th} element of $\mathbf{a}(\varphi)$ is given by

$$a_l(\varphi) = \exp\{j\psi_l(\varphi)\}, \quad l \in \mathrm{S} \tag{17}$$

[‡‡]Ideal steering vectors are assumed for both UCAs. In practice, we can accurately consider the effect of mutual coupling between the antennas and the platform structures, either by measuring the steering vectors of the UCAs in a suitable test range using controlled RF transmissions [3], [35] or by estimating them using the computational EM solver with a fairly accurate model of the platform structure and the antenna array.

where

$$\psi_l(\varphi) = \psi'_m(\varphi) - \psi''_n(\varphi), \; l \in \mathrm{S}, \; m \in \mathrm{S}'_1, \; n \in \mathrm{S}''_2. \tag{18}$$

In (18), the indices l are generated by enumerating through the indices m and n. For each m, we enumerate the index n for each sequential increment in l starting from a value of 1. The relations among the indices can be expressed as follows.

$$\begin{aligned} &l = (m-1)N + n, \; l \in \mathrm{S}, \\ &n = l \bmod (N), \, m = \frac{(l-n)}{N} + 1, \\ &m \in \mathrm{S}'_1, \; n \in \mathrm{S}''_2. \end{aligned} \tag{19}$$

(18) can be further simplified to obtain a useful geometrical interpretation of the underlying difference co-array structure. We have

$$\begin{aligned} \psi_l(\varphi) = \frac{2\pi}{\lambda}\left[R_1\cos\left(\nu'_m - \varphi\right) - R_2\cos\left(\nu''_n - \varphi\right)\right], \\ l \in \mathrm{S}, \, , \; m \in \mathrm{S}'_1, \; n \in \mathrm{S}''_2. \end{aligned} \tag{20}$$

After some algebraic manipulations, we can rewrite the equation given above as

$$\psi_l(\varphi) = \frac{2\pi r_l}{\lambda}\left[\cos\left(\zeta_l - \varphi\right)\right], \; l \in \mathrm{S}, \tag{21}$$

where

$$r_l = \sqrt{\Upsilon_{mn}^2 + \Omega_{mn}^2}, \quad l \in \mathrm{S}, \; m \in \mathrm{S}'_1, \; n \in \mathrm{S}''_2, \tag{22}$$

and

$$\tan(\zeta_l) = \frac{\Omega_{mn}}{\Upsilon_{mn}}, \quad l \in \mathrm{S}, \; m \in \mathrm{S}'_1, \; n \in \mathrm{S}''_2, \tag{23}$$

with $\Upsilon_{mn} = \left(R_1\cos\nu'_m - R_2\cos\nu''_n\right)$ and $\Omega_{mn} = \left(R_1\sin\nu'_m - R_2\sin\nu''_n\right)$.

Based on (21) to (23), we can geometrically interpret that the l^{th} element of the difference co-array lies on a circle of radius r_l with an angular displacement of ζ_l. A four-quadrant inverse tangent function must be used to obtain the value of ζ_l in (23). We show the array geometry of CCUCA and NSCA [48] in Fig. 2. The geometries of their corresponding difference co-arrays, owing to the cross terms, are shown in Fig. 3. From these figures, it can be observed that the difference co-array has an aperture that is approximately the sum of the apertures of the two physical arrays and is densely filled with virtual sensors, in contrast to the total number of physical sensors. Thus, a larger aperture and a higher number of virtual sensors result in an improved DOA estimation performance when a difference co-array is exploited.

C. MATHEMATICAL SIGNAL MODEL OF DIFFERENCE CO-ARRAY OF CCUCA

We develop a mathematical signal model for the data received by the difference co-array of the CCUCA. We make the following assumptions.

i. The number of far-field radio sources Q is known.

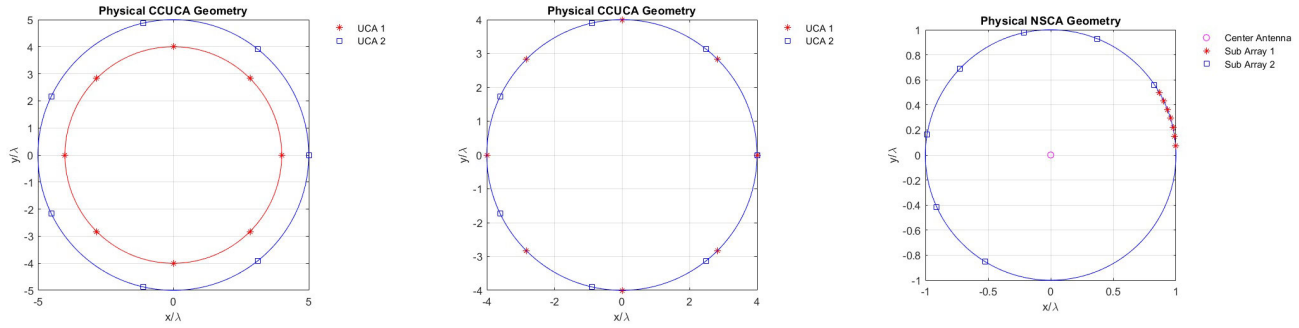

(a) (b) (c)

FIGURE 2. (a) CCUCA geometry with $R_1 = 4\lambda$, $R_2 = 5\lambda$, $M = 3$, $N = 7$ (b) CCUCA geometry with $R_1 = 4\lambda$, $R_2 = 4\lambda$, $M = 3$, $N = 7$ (c) NSCA geometry with 15 antennas and radius = λ.

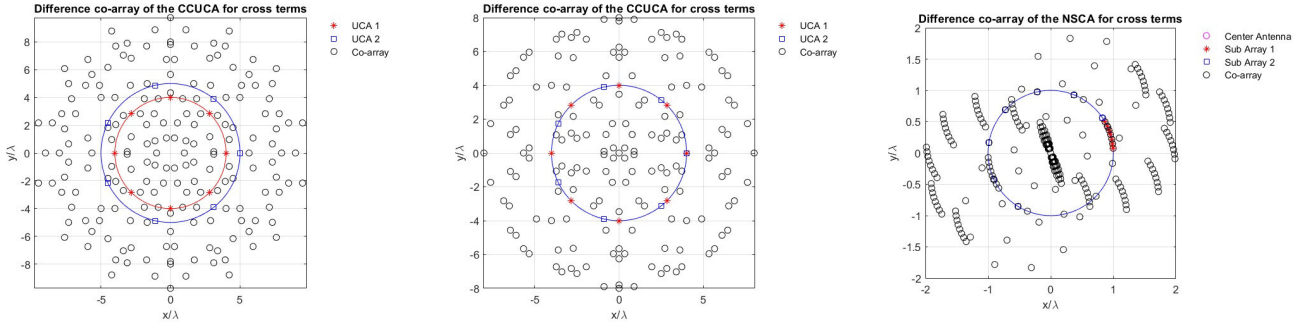

(a) (b) (c)

FIGURE 3. (a) CCUCA difference co-array with $R_1 = 4\lambda$, $R_2 = 5\lambda$, $M = 3$, $N = 7$ (b) CCUCA difference co-array with $R_1 = 4\lambda$, $R_2 = 4\lambda$, $M = 3$, $N = 7$ (c) NSCA difference co-array with 15 antennas and radius = λ.

ii. These Q far-field radio sources radiate zero-mean narrowband signals with wavelength λ and complex envelopes $s_1(t), s_2(t), \ldots, s_Q(t)$. $s_i(t)$ denotes the complex signal envelope received from the i^{th} source at the CCUCA phase center. The signals are uncorrelated and $\mathbb{E}\{|s_i(t)|^2\} = \sigma_i^2$, $i = 1, 2, \cdots, Q$. We stack the signals in a signal vector $\mathbf{s}(t) = \left[s_1(t)\ s_2(t) \ldots\ s_Q(t)\right]^T$.

iii. The azimuth angles of the Q sources are denoted by $\varphi_1, \varphi_2 \ldots, \varphi_Q$, which lie on a grid, and their corresponding elevation angles with respect to the X-Y plane are set to $\theta = 0°$.

iv. The noise at each antenna is not correlated with the noise at the other antennas or with the source signals. We denote the additive noise vectors at UCA 1 and UCA 2 by $\mathbf{n}_1(t)$ and $\mathbf{n}_2(t)$, respectively. The elements of $\mathbf{n}_1(t)$ and $\mathbf{n}_2(t)$ are modeled as independent and identically distributed (i.i.d.) complex Gaussian random variables with zero mean and variance σ_w^2. Therefore, $\mathbf{n}_1(t) \sim \mathcal{CN}\left(\mathbf{0}, \sigma_w^2 \mathbf{I}_{(3M-1)}\right)$, and $\mathbf{n}_2(t) \sim \mathcal{CN}\left(\mathbf{0}, \sigma_w^2 \mathbf{I}_N\right)$.

v. Each antenna in the array is connected to its own RF receiver chain. All receiver chains, followed by their corresponding analog-to-digital converters (ADCs) used to sample the signals, are phase-coherent. In practice, gain and phase mismatches exist between the channels in RF chains and ADCs, which are calibrated throughout the operational frequency range [35], [52].

The data vectors $\mathbf{x}_1(t) \in \mathbb{C}^{3M-1}$ and $\mathbf{x}_2(t) \in \mathbb{C}^N$ received at UCA 1 and UCA 2, respectively, at time t can be expressed as [2], [3], and [5],

$$\begin{aligned}\mathbf{x}_1(t) &= \sum_{q=1}^{Q} \mathbf{a}_1(\varphi_q) s_q(t) + \mathbf{n}_1(t) \\ &= \mathbf{A}_1 \mathbf{s}(t) + \mathbf{n}_1(t), \end{aligned} \tag{24}$$

$$\begin{aligned}\mathbf{x}_2(t) &= \sum_{q=1}^{Q} \mathbf{a}_2(\varphi_q) s_q(t) + \mathbf{n}_2(t) \\ &= \mathbf{A}_2 \mathbf{s}(t) + \mathbf{n}_2(t), \end{aligned} \tag{25}$$

where $\mathbf{A}_1 = \left[\mathbf{a}_1(\varphi_1)\ \mathbf{a}_1(\varphi_2) \ldots \mathbf{a}_1(\varphi_Q)\right]$ is the $(3M - 1) \times Q$ manifold matrix of UCA 1 and $\mathbf{A}_2 = \left[\mathbf{a}_2(\varphi_1)\ \mathbf{a}_2(\varphi_2) \ldots \mathbf{a}_2(\varphi_Q)\right]$ is the $N \times Q$ manifold matrix of UCA 2. The steering vector of UCA 1 is given by

$$\mathbf{a}_1(\varphi) = \left[a_1'(\varphi)\ a_2'(\varphi)\ \cdots\ a_{3M-1}'(\varphi)\right]^T \tag{26}$$

and that of UCA 2 is given by

$$\mathbf{a}_2(\varphi) = \left[a_1''(\varphi)\ a_2''(\varphi)\ \cdots\ a_N''(\varphi)\right]^T \tag{27}$$

where

$$a'_m(\varphi) = \exp\left\{\frac{j2\pi R_1}{\lambda}\cos\left[\nu'_m - \varphi\right]\right\}, m \in S'_1$$

and,

$$a''_n(\varphi) = \exp\left\{\frac{j2\pi R_2}{\lambda}\cos\left[\nu''_n - \varphi\right]\right\}, n \in S''_2.$$

The cross covariance matrix between the received data vectors $\mathbf{x}_1(t)$ and $\mathbf{x}_2(t)$ can be expressed as

$$\begin{aligned}\mathbf{R}_{x_{12}} &= \mathbb{E}\left\{\mathbf{x}_1(t)\mathbf{x}_2^H(t)\right\} = \mathbf{A}_1\mathbf{R}_{ss}\mathbf{A}_2^H \\ &= \sum_{q=1}^{Q}\sigma_q^2\mathbf{a}_1(\varphi_q)\mathbf{a}_2^H(\varphi_q),\end{aligned} \tag{28}$$

where $\mathbf{R}_{ss} = \text{diag}(\sigma_1^2, \sigma_2^2, \ldots, \sigma_Q^2)$ is the covariance matrix of the source signals. We observe that in (28), there is no contribution from noise. In practice, $\mathbf{R}_{x_{12}}$ is estimated using T available snapshots of $\{\mathbf{x}_1(t)\}$ and $\{\mathbf{x}_2(t)\}$ for $t = 0, 1, \cdots, T-1$,[‡] as follows.

$$\widehat{\mathbf{R}}_{x_{12}} = \frac{1}{T}\sum_{t=0}^{T-1}\mathbf{x}_1(t)\mathbf{x}_2^H(t). \tag{29}$$

DOA estimation using a difference co-array requires vectorizing of the cross covariance matrix. If $Q < \min(N, 3M-1)$, then we can retain the Q principal components by using a rank-reduced approximation of the sample cross covariance matrix $\widehat{\mathbf{R}}_{x_{12}}$, denoted by $\widetilde{\mathbf{R}}_{x_{12}}$. We proceed by exploiting the inherent structure of the problem through the singular value decomposition (SVD) [54] of $\widehat{\mathbf{R}}_{x_{12}} \in \mathbb{C}^{(3M-1)\times N}$ expressed as

$$\widehat{\mathbf{R}}_{x_{12}} = \mathbf{U}_{12}\mathbf{\Sigma}_{12}\mathbf{V}_{12}^H, \tag{30}$$

where $\mathbf{U_{12}}$, $\mathbf{V_{12}}$ are unitary matrices and $\mathbf{\Sigma_{12}}$ is a diagonal matrix of singular values. This decomposition allows the separation of the signal and noise subspaces. $\widetilde{\mathbf{R}}_{x_{12}}$ is computed by retaining the Q largest singular values in $\mathbf{\Sigma_{12}}$ and the corresponding columns in $\mathbf{U_{12}}$ and $\mathbf{V_{12}}$. This 'denoising' operation can be represented as

$$\begin{aligned}\widetilde{\mathbf{R}}_{x_{12}} = \mathbf{U}_{12}(:, 1:Q)\,\mathbf{\Sigma}_{12}(1:Q, 1:Q)\,\mathbf{V}_{12}^H(:, 1:Q), \\ Q < \min(N,\ 3M-1).\end{aligned} \tag{31}$$

Whenever $Q \geq \min(N, 3M-1)$, it is not feasible to obtain a rank-reduced approximation of $\widehat{\mathbf{R}}_{x_{12}}$. Because there is no need to compute the SVD of $\widehat{\mathbf{R}}_{x_{12}}$ in this case, we set $\widetilde{\mathbf{R}}_{x_{12}} = \widehat{\mathbf{R}}_{x_{12}}$ and proceed accordingly. Vectorizing matrix $\widetilde{\mathbf{R}}_{x_{12}}$ allows the measurement vector $\mathbf{z}$ to be expressed as

$$\mathbf{z} = vec(\widetilde{\mathbf{R}}_{x_{12}}) = \bar{\mathbf{A}}\mathbf{b}, \tag{32}$$

where

$$\mathbf{b} = \left[\sigma_1^2 \ldots \sigma_Q^2\right]^T \tag{33}$$

and $\bar{\mathbf{A}} = \left[\bar{\mathbf{a}}(\varphi_1) \cdots \bar{\mathbf{a}}(\varphi_Q)\right]$ with

$$\bar{\mathbf{a}}(\varphi) = \mathbf{a}_1(\varphi) \otimes \mathbf{a}_2^*(\varphi). \tag{34}$$

The data model expressed in (32) to (34) allows us to interpret the elements of $\mathbf{z}$ as the samples received by the difference co-array. In particular, we consider the vector $\mathbf{b} \in \mathbb{C}^Q$ in (32) as a single snapshot signal vector, and $\bar{\mathbf{A}}$ as the manifold matrix of the difference co-array.

III. AZIMUTH DOA ESTIMATION WITH CCUCA USING SPARSE BAYESIAN LEARNING

In this section, we describe the proposed algorithm for azimuth DOA estimation using the SBL on the data received by the difference co-array of the CCUCA. Equation (32) represents an inverse problem in which both $\bar{\mathbf{A}}$ and $\mathbf{b}$ are unknown and need to be estimated. Sparse signal recovery techniques [8], [30], [31], [32] such as orthogonal matching pursuit (OMP), basis pursuit denoising (BPDN), Bayesian hierarchical learning techniques such as SBL *etc.* are potential methods for this estimation. Unlike subspace-based approaches, sparse recovery techniques can also deal with correlated sources [6], [20], [21]. The sparse representation of the measurement vector $\mathbf{z}$ in the spatial *i.e.*, 'azimuth' domain is obtained using a dictionary $\mathbf{\Phi}$ in the form $\mathbf{z} = \mathbf{\Phi p}$ [8], [9], [55]. The g^{th} column of $\mathbf{\Phi}$ is denoted by $\mathbf{\Phi}(:, g)$, and equals $\bar{\mathbf{a}}(\varphi_g)$ as given in (34). The index g corresponds to φ_g, a grid point in the azimuth space $S_\varphi \subseteq [0,\ 2\pi]$. Usually in practice, the step size between consecutive grid points is close to 1°. The "atoms" of the dictionary are the steering vectors at the grid points. We assume that $|S_\varphi| = G$ and denote $S_\varphi \overset{\text{def}}{=} \{\varphi_1, \varphi_2, \cdots, \varphi_G\}$, and therefore $\mathbf{p} \in \mathbb{C}^G$. The sparse recovery problem is therefore to determine the Q-sparse vector $\mathbf{p}$ that lies in a G-dimensional subspace with $Q \ll G$. The Q azimuth DOAs are then obtained from the indices of Q largest peaks in $|\mathbf{p}|$.

The process followed in OMP and BPDN to recover the Q-sparse vector $\mathbf{p}$ promotes sparsity starting from the minimum order by retaining the strongest component [9]. The sparsity is gradually increased until the true sparsity is attained. In contrast, the SBL recovery process proceeds in the opposite direction. Sparsity is iteratively reduced from the maximum value to the true value [9]. A fine azimuth grid smaller than 1° leads to mutual coherence among the steering vectors of adjacent azimuth angles. This coherence disrupts the Restricted Isometry Property (RIP) [8]. This limitation is usually handled by resorting to off-grid DOA estimation techniques [38], [56]. However, handling of off-grid DOAs is not within the scope of this study.

In such situations, a Bayesian approach, such as SBL performs better than OMP and BPDN, although at the loss of convexity. SBL generally presents several benefits: it is more robust to noise and does not require tuning of regularization parameters. It infers both the sparsity level and noise variance directly from the data in contrast to OMP. It also naturally extends to block-sparsity scenarios

[‡]In this study, we use an integer to represent the time instant t. This corresponds to the discrete time $\frac{t}{F_s}$, where F_s is the sampling frequency for the complex envelope of the received narrowband signal [53], as per the Nyquist sampling theorem.

and provides complete posterior parameter information rather than point estimates. The Bayesian parameter estimation point of view introduces a hierarchical data model in which the unknown Q-sparse vector $\mathbf{p}$ is treated as a zero mean complex Gaussian random vector with an unknown diagonal covariance $\mathbf{\Gamma} = \text{diag}(\gamma_1, \gamma_2, \cdots, \gamma_G)$, *i.e.*, $\mathbf{p} \sim \mathcal{CN}(\mathbf{0}, \mathbf{\Gamma})$. The hyperparameters are the variances γ_g, $g \in S_G$ with $S_G \stackrel{\text{def}}{=} \{1, 2, \cdots, G\}$. The use of hierarchical models with appropriate choices for priors promotes sparsity.

In SBL, a reasonable assumption is a Gaussian model for the priors and the likelihood for mathematical tractability [9], [30], [32]. The linear observation model is expressed as follows.

$$\mathbf{z} = \mathbf{\Phi}\mathbf{p} + \boldsymbol{\epsilon}, \tag{35}$$

where the noise vector $\boldsymbol{\epsilon} \sim \mathcal{CN}\left(\mathbf{0}, \sigma^2 \mathbf{I}_{L_z}\right)$. It is reasonable to assume that $\boldsymbol{\epsilon}$ is uncorrelated with the Q-sparse vector $\mathbf{p}$. The prior for the Gaussian model [57] with hyperparameters encoded in $\mathbf{\Gamma}$ is given by

$$f(\mathbf{p}|\mathbf{\Gamma}) = \frac{1}{(\pi)^G |\mathbf{\Gamma}|} \exp\left(-\mathbf{p}^H \mathbf{\Gamma}^{-1} \mathbf{p}\right) \tag{36}$$

and the likelihood distribution is given by

$$f\left(\mathbf{z}|\mathbf{p}, \sigma^2\right) = \frac{1}{\left(\pi\sigma^2\right)^{L_z}} \exp\left(-\frac{\|\mathbf{z} - \mathbf{\Phi}\mathbf{p}\|^2}{\sigma^2}\right). \tag{37}$$

It follows from the linear data model in (35) that if $\mathbf{\Gamma}$ and σ^2 are known, then $\mathbf{z} \sim \mathcal{CN}(\mathbf{0}, \mathbf{\Sigma}_z)$, where

$$\mathbf{\Sigma}_z = \sigma^2 \mathbf{I}_{L_z} + \mathbf{\Phi}\mathbf{\Gamma}\mathbf{\Phi}^H \tag{38}$$

has the dimension L_z x L_z with $L_z = |\{\mathbf{z}\}| = (3M - 1)N$. Thus, for Gaussian priors and likelihood, the *evidence*, i.e., the marginal distribution of the measurement vector, also has a Gaussian distribution. Therefore,

$$f\left(\mathbf{z}|\mathbf{\Gamma}, \sigma^2\right) = \frac{1}{(\pi)^{L_z} |\mathbf{\Sigma}_z|} \exp\left(-\mathbf{z}^H \mathbf{\Sigma}_z{}^{-1} \mathbf{z}\right). \tag{39}$$

The posterior distribution of $\mathbf{p}$, given, $\mathbf{z}$, $\mathbf{\Gamma}$, and model noise variance σ^2 is,

$$\begin{aligned} f\left(\mathbf{p}|\mathbf{z}, \mathbf{\Gamma}, \sigma^2\right) &= \frac{f\left(\mathbf{p}, \mathbf{z}, \mathbf{\Gamma}, \sigma^2\right)}{f\left(\mathbf{z}, \mathbf{\Gamma}, \sigma^2\right)} \\ &= \frac{f\left(\mathbf{z}|\mathbf{p}, \mathbf{\Gamma}, \sigma^2\right) f\left(\mathbf{p}, \mathbf{\Gamma}, \sigma^2\right)}{f\left(\mathbf{z}|\mathbf{\Gamma}, \sigma^2\right) f\left(\mathbf{\Gamma}, \sigma^2\right)} \\ &= \frac{f\left(\mathbf{z}|\mathbf{p}, \sigma^2\right) f\left(\mathbf{p}|\mathbf{\Gamma}\right)}{f\left(\mathbf{z}|\mathbf{\Gamma}, \sigma^2\right)}. \end{aligned} \tag{40}$$

Since $\mathbf{\Gamma}$ and σ^2 are unknown, marginalization with respect to these variables leads to the following simplification:

$$\begin{aligned} f(\mathbf{p}|\mathbf{z}) &= \frac{f(\mathbf{p}, \mathbf{z})}{f(\mathbf{z})} \\ &= \frac{1}{f(\mathbf{z})} \int_0^\infty f\left(\mathbf{p}|\mathbf{z}, \mathbf{\Gamma}, \sigma^2\right) f\left(\mathbf{z}, \mathbf{\Gamma}, \sigma^2\right) d\mathbf{\Gamma} d\sigma^2 \\ &= \int_0^\infty f\left(\mathbf{p}|\mathbf{z}, \mathbf{\Gamma}, \sigma^2\right) f\left(\mathbf{\Gamma}, \sigma^2|\mathbf{z}\right) d\mathbf{\Gamma} d\sigma^2. \end{aligned} \tag{41}$$

The second term of the integrand in (41) is the evidence for $\mathbf{\Gamma}$ and σ^2 in the data. When the evidence peaks at the true values $\mathbf{\Gamma}_{ev}$ and σ^2_{ev}, then $f\left(\mathbf{\Gamma}, \sigma^2|\mathbf{z}\right) = \delta\left(\mathbf{\Gamma}_{ev}, \sigma^2_{ev}\right)$. Therefore, we can make the following approximation for the true posterior distribution:

$$f(\mathbf{p}|\mathbf{z}) \approx f\left(\mathbf{p}|\mathbf{z}, \mathbf{\Gamma}_{ev}, \sigma^2_{ev}\right). \tag{42}$$

We observe that since

$$f\left(\mathbf{\Gamma}, \sigma^2|\mathbf{z}\right) \propto f\left(\mathbf{z}|\mathbf{\Gamma}, \sigma^2\right) f(\mathbf{\Gamma}) f\left(\sigma^2\right), \tag{43}$$

for flat hyperpriors, we must determine the maximum of

$$f\left(\mathbf{z}|\mathbf{\Gamma}, \sigma^2\right) = \int_{-\infty}^{\infty} f\left(\mathbf{z}|\mathbf{p}, \sigma^2\right) f(\mathbf{p}|\mathbf{\Gamma})\, d\mathbf{p}. \tag{44}$$

It can be seen that the integrand of (44) is the numerator of the posterior distribution given in (40). Using (36) and (37), the exponent of the integrand in (44) can be expressed as

$$h(\mathbf{p}) = -\frac{1}{\sigma^2} (\mathbf{z} - \mathbf{\Phi}\mathbf{p})^H (\mathbf{z} - \mathbf{\Phi}\mathbf{p}) - \mathbf{p}^H \mathbf{\Gamma}^{-1} \mathbf{p}. \tag{45}$$

The value of $\mathbf{p}$ that maximizes the concave expression above can be determined by equating the gradient of (45) to zero. Doing this yields $\tilde{\mathbf{p}}$, the maximizer of $h(\mathbf{p})$ as

$$\tilde{\mathbf{p}} = \mathbf{\Sigma}^{-1} \mathbf{\Phi}^H \mathbf{z}, \tag{46}$$

where

$$\mathbf{\Sigma} = \left(\mathbf{\Phi}^H \mathbf{\Phi} + \sigma^2 \mathbf{\Gamma}^{-1}\right). \tag{47}$$

The inverse of matrix $\mathbf{\Sigma}$ exists with a very high probability because it is the sum of an invertible matrix $\sigma^2 \mathbf{\Gamma}^{-1}$ and a Gram matrix of dictionary $\mathbf{\Phi}$. By adding and subtracting the quantity, $\frac{1}{\sigma^2} \tilde{\mathbf{p}}^H \mathbf{\Sigma} \tilde{\mathbf{p}}$, we can complete the squares in (45). After some algebraic manipulations, we can express the exponent of the integrand in (44) as

$$h(\mathbf{p}) = -\frac{1}{\sigma^2} \left[\mathbf{z}^H \mathbf{z} - \tilde{\mathbf{p}}^H \mathbf{\Sigma} \tilde{\mathbf{p}} + (\mathbf{p} - \tilde{\mathbf{p}})^H \mathbf{\Sigma} (\mathbf{p} - \tilde{\mathbf{p}})\right]. \tag{48}$$

Using the properties of integrals of multivariate Gaussians and from (44) and (48), we can express the "evidence integral" or the "marginal likelihood" as

$$\begin{aligned} f\left(\mathbf{z}|\mathbf{\Gamma}, \sigma^2\right) &= \int_{-\infty}^{\infty} f\left(\mathbf{z}|\mathbf{p}, \sigma^2\right) f(\mathbf{p}|\mathbf{\Gamma})\, d\mathbf{p} \\ &= \frac{|\mathbf{\Sigma}^{-1}|}{C' |\mathbf{\Gamma}|} \exp\left(-\frac{\left[\mathbf{z}^H \mathbf{z} - \tilde{\mathbf{p}}^H \mathbf{\Sigma} \tilde{\mathbf{p}}\right]}{\sigma^2}\right), \end{aligned} \tag{49}$$

where C' is a nonzero constant. In SBL, which is based on the empirical Bayes approach, we solve the following optimization problem to obtain point estimates of $\mathbf{\Gamma}$ and σ^2:

$$\begin{aligned} \left\{\mathbf{\Gamma}_{ev}, \sigma^2_{ev}\right\} &= \arg\max_{\mathbf{\Gamma}, \sigma^2} \left\{f\left(\mathbf{z}|\mathbf{\Gamma}, \sigma^2\right)\right\} \\ &= \arg\max_{\mathbf{\Gamma}, \sigma^2} \left\{\log\left(f\left(\mathbf{z}|\mathbf{\Gamma}, \sigma^2\right)\right)\right\} \end{aligned}$$

$$= \arg\max_{\mathbf{\Gamma},\sigma^2} \left\{ -\log\left(|\mathbf{\Sigma\Gamma}|\right) + \frac{\tilde{\mathbf{p}}^H \mathbf{\Sigma} \tilde{\mathbf{p}} - \mathbf{z}^H \mathbf{z}}{\sigma^2} \right\}, \tag{50}$$

where the constant term independent of $\mathbf{\Gamma}$ and σ^2 is ignored. The likelihood or cost function in (50) is denoted as

$$\begin{aligned} J\left(\mathbf{\Gamma}, \sigma^2\right) &\stackrel{\text{def}}{=} \left\{ -\log\left(|\mathbf{\Sigma\Gamma}|\right) + \frac{\tilde{\mathbf{p}}^H \mathbf{\Sigma} \tilde{\mathbf{p}} - \mathbf{z}^H \mathbf{z}}{\sigma^2} \right\}, \\ &= J_1\left(\mathbf{\Gamma}, \sigma^2\right) + J_2\left(\mathbf{\Gamma}, \sigma^2\right), \end{aligned} \tag{51}$$

with,

$$\begin{aligned} J_1\left(\mathbf{\Gamma}, \sigma^2\right) &= -\log\left(|\mathbf{\Sigma\Gamma}|\right), \\ J_2\left(\mathbf{\Gamma}, \sigma^2\right) &= \frac{\tilde{\mathbf{p}}^H \mathbf{\Sigma} \tilde{\mathbf{p}} - \mathbf{z}^H \mathbf{z}}{\sigma^2}. \end{aligned} \tag{52}$$

Referring to (39), we see that $\mathbf{\Gamma}$ and σ^2 can also be estimated from the measurements by solving the following optimization problem, which maximizes the log of evidence [32].

$$\left\{\mathbf{\Gamma}_{ev}, \sigma^2_{ev}\right\} = \arg\max_{\mathbf{\Gamma},\sigma^2} \left\{ -\mathbf{z}^H {\mathbf{\Sigma}_z}^{-1} \mathbf{z} - \log|\mathbf{\Sigma}_z| \right\}. \tag{53}$$

Let $J'\left(\mathbf{\Gamma}, \sigma^2\right) \stackrel{\text{def}}{=} \left\{ -\mathbf{z}^H {\mathbf{\Sigma}_z}^{-1} \mathbf{z} - \log|\mathbf{\Sigma}_z| \right\}$ denote the objective function in (53). We observe that $J'\left(\mathbf{\Gamma}, \sigma^2\right)$ is non-convex. The following Lemma is used to prove that the objective functions of the optimization problems given in (50) and (53) are equivalent.

Lemma 1: $J\left(\mathbf{\Gamma}, \sigma^2\right) = J'\left(\mathbf{\Gamma}, \sigma^2\right)$.

Proof: We prove this equivalence using the matrix inversion lemma and properties of the matrix determinants [58]. $J_1\left(\mathbf{\Gamma}, \sigma^2\right)$ can be simplified using the properties of the matrix determinants as follows.

$$\begin{aligned} |\mathbf{\Sigma\Gamma}| &= \left|\left(\mathbf{\Phi}^H\mathbf{\Phi} + \sigma^2\mathbf{\Gamma}^{-1}\right)\right| |\mathbf{\Gamma}| \\ &= \left|\sigma^2\mathbf{\Gamma}^{-1}\right| \left|\mathbf{I}_{L_z} + \sigma^{-2}\mathbf{\Phi\Gamma\Phi}^H\right| |\mathbf{\Gamma}| \\ &= \left|\sigma^2\mathbf{\Gamma}^{-1}\right| \left|\sigma^2\mathbf{I}_{L_z} + \mathbf{\Phi\Gamma\Phi}^H\right| \left|\sigma^{-2}\mathbf{I}_G\right| |\mathbf{\Gamma}| \\ &= \left|\sigma^2\mathbf{I}_{L_z} + \mathbf{\Phi\Gamma\Phi}^H\right| \\ &= |\mathbf{\Sigma}_z| \end{aligned} \tag{54}$$

Similarly, using (46) and (47), $J_2\left(\mathbf{\Gamma}, \sigma^2\right)$ can be simplified as

$$\begin{aligned} J_2\left(\mathbf{\Gamma}, \sigma^2\right) &= \frac{1}{\sigma^2}\left\{\mathbf{z}^H\mathbf{\Phi}\mathbf{\Sigma}^{-1}\mathbf{\Phi}^H\mathbf{z} - \mathbf{z}^H\mathbf{z}\right\} \\ &= \frac{1}{\sigma^2}\mathbf{z}^H\left\{\mathbf{\Phi}\mathbf{\Sigma}^{-1}\mathbf{\Phi}^H - \mathbf{I}_{L_z}\right\}\mathbf{z} \\ &= -\mathbf{z}^H {\mathbf{\Sigma}_z}^{-1}\mathbf{z}, \end{aligned} \tag{55}$$

where we used the fact that

$$\begin{aligned} {\mathbf{\Sigma}_z}^{-1} &= \left\{\sigma^2\mathbf{I}_{Lz} + \mathbf{\Phi\Gamma\Phi}^H\right\}^{-1} \\ &= \frac{1}{\sigma^2}\left[\mathbf{I}_{Lz} - \mathbf{\Phi}\left(\mathbf{\Phi}^H\mathbf{\Phi} + \sigma^2\mathbf{\Gamma}^{-1}\right)^{-1}\mathbf{\Phi}^H\right] \\ &= \frac{1}{\sigma^2}\left[\mathbf{I}_{L_z} - \mathbf{\Phi}\mathbf{\Sigma}^{-1}\mathbf{\Phi}^H\right]. \end{aligned} \tag{56}$$

Substituting (52) through (56) into (51) shows that $J\left(\mathbf{\Gamma}, \sigma^2\right) = J'\left(\mathbf{\Gamma}, \sigma^2\right)$. ■

Since we use the Maximum Likelihood (ML) estimates of $\mathbf{\Gamma}$ and σ^2, in the posterior distribution given in (42), this procedure is called Type II ML. Due to the Gaussian model assumption [57], we can express the posterior pdf $f\left(\mathbf{p}|\mathbf{z}\right)$ as

$$f\left(\mathbf{p}|\mathbf{z}\right) \sim \mathcal{CN}\left(\boldsymbol{\mu}, \mathbf{\Sigma}\right), \tag{57}$$

with,

$$\begin{aligned} \mathbf{\Sigma} &= \left(\mathbf{\Phi}^H\mathbf{\Phi} + \sigma^2_{ev}\mathbf{\Gamma}^{-1}_{ev}\right) \\ \boldsymbol{\mu} &= \tilde{\mathbf{p}} = \mathbf{\Sigma}^{-1}\mathbf{\Phi}^H\mathbf{z} = \mathbf{\Gamma}_{ev}\mathbf{\Phi}^H{\mathbf{\Sigma}_z}^{-1}\mathbf{z}, \end{aligned} \tag{58}$$

where we have used the matrix inversion lemma [58].

Thus, the maximum a posteriori (MAP) estimate of $\mathbf{p}$ is given by the mean of the posterior, *i.e.*, $\boldsymbol{\mu}$. A careful examination of (58), (53), and (50) reveals the need for an iterative solution. We propose an algorithm for the iterative solution. This algorithm is similar to the approach used in [31] and [32]. We start with an initial value of $\mathbf{\Gamma}$ and σ^2 and estimate $\mathbf{\Sigma}_z$. Using this new value of $\mathbf{\Sigma}_z$, we next update the values of $\mathbf{\Gamma}$ and σ^2. This process proceeds iteratively until the convergence or completion of the maximum number of iterations. We finally obtain the sparse solution for $\mathbf{p}$ as the mean of the posterior distribution given in (58). The posterior distribution itself completely models the uncertainty in $\mathbf{p}$.

The update rule for γ_g, the g^{th} diagonal element of $\mathbf{\Gamma}$ can be analytically obtained [31], [32] by setting the partial derivative of $J'\left(\mathbf{\Gamma}, \sigma^2\right)$ with respect to γ_g to zero, $\forall g \in S_G$. Using the rules of matrix differentiation by scalar [59] along with the constraint imposed by the model that $\mathbf{\Gamma}$ is diagonal, we obtain the following.

$$\begin{aligned} \frac{\partial J'\left(\mathbf{\Gamma}, \sigma^2\right)}{\partial \gamma_g} &= -\frac{\partial\left(\mathbf{z}^H{\mathbf{\Sigma}_z}^{-1}\mathbf{z}\right)}{\partial\gamma_g} - \frac{\partial \log|\mathbf{\Sigma}_z|}{\partial\gamma_g} \\ &= \mathbf{z}^H{\mathbf{\Sigma}_z}^{-1}\frac{\partial\mathbf{\Sigma}_z}{\partial\gamma_g}{\mathbf{\Sigma}_z}^{-1}\mathbf{z} - Tr\left\{{\mathbf{\Sigma}_z}^{-1}\frac{\partial\mathbf{\Sigma}_z}{\partial\gamma_g}\right\} \\ &= \left\|\mathbf{z}^H{\mathbf{\Sigma}_z}^{-1}\mathbf{\Phi}\left(:,g\right)\right\|_2^2 \\ &\quad - \mathbf{\Phi}\left(:,g\right)^H{\mathbf{\Sigma}_z}^{-1}\mathbf{\Phi}\left(:,g\right) \\ &= \left(\frac{\gamma_g^{old}}{\gamma_g}\right)^2\left\|\mathbf{z}^H{\mathbf{\Sigma}_z}^{-1}\mathbf{\Phi}\left(:,g\right)\right\|_2^2 \\ &\quad - \mathbf{\Phi}\left(:,g\right)^H{\mathbf{\Sigma}_z}^{-1}\mathbf{\Phi}\left(:,g\right), \forall g \in S_G. \end{aligned} \tag{59}$$

We introduce the factor $\left(\frac{\gamma_g^{old}}{\gamma_g}\right)^2$ in (59) to obtain an iterative equation in γ_g. Assuming that we know γ_g and $\mathbf{\Sigma}_z$ from the previous iteration or initialization, and setting $\frac{\partial J'\left(\mathbf{\Gamma}, \sigma^2\right)}{\partial\gamma_g}$ to zero, we obtain the update rule as

$$\gamma_g = \frac{\gamma_g^{old}\left\|\mathbf{z}^H{\mathbf{\Sigma}_z}^{-1}\mathbf{\Phi}\left(:,g\right)\right\|_2}{\sqrt{\mathbf{\Phi}\left(:,g\right)^H{\mathbf{\Sigma}_z}^{-1}\mathbf{\Phi}\left(:,g\right)}}, \quad \forall g \in S_G. \tag{60}$$

The convergence of the SBL algorithm depends on the use of a good estimate of noise variance, σ^2. We propose updating σ^2 using the asymptotically efficient estimate of noise variance derived in [31]. This estimate is based on stochastic ML for Q sources and is given by

$$\sigma^2 = \frac{1}{L_z - Q} Tr\left\{\left(\mathbf{I}_{L_z} - \boldsymbol{\Psi}\boldsymbol{\Psi}^{\dagger}\right)\mathbf{z}\mathbf{z}^H\right\}, \tag{61}$$

where

$$\boldsymbol{\Psi} = \boldsymbol{\Phi}\left(:, \Re_c\right), \tag{62}$$

and

$$\boldsymbol{\Psi}^{\dagger} = \left(\boldsymbol{\Psi}^H\boldsymbol{\Psi}\right)^{-1}\boldsymbol{\Psi}^H. \tag{63}$$

In (62), the columns of the dictionary matrix indexed by the set $\Re_c$ corresponding to Q largest peaks in $\boldsymbol{\gamma}$ are used to construct the manifold matrix $\boldsymbol{\Psi}$ which is used to estimate the orthogonal complement of the projection matrix given by $\left(\mathbf{I}_{L_z} - \boldsymbol{\Psi}\boldsymbol{\Psi}^{\dagger}\right)$. This estimate of σ^2 is asymptotically efficient because $\widehat{\mathbf{R}}_{x_{12}} \to \mathbf{R}_{x_{12}}$, whenever, $T \to \infty$. At the optimal solution, $\boldsymbol{\Psi}^H\left(\mathbf{z}\mathbf{z}^H - \boldsymbol{\Sigma}_z\right)\boldsymbol{\Psi} = \mathbf{0}$ which is Jaffer's necessary condition [60].

The description of the proposed SBL algorithm is presented in Algorithm 1. The algorithm computes an index set $\Re_c$, corresponding to the Q largest peaks in $\boldsymbol{\gamma}$, using which the estimated azimuth DOA of the sources is $S_\varphi\left(\Re_c\right)$. An estimate of the number of computations in terms of complex multiplications, denoted by $\mathfrak{M}$, and complex additions, denoted by $\mathfrak{A}$, required for the algorithm is provided in Appendix.

From (A-1) to (A-4), we observe that the total number of computations depends on the size of the grid, G, the number of sources, Q, the dimension of the difference co-array, $L_z = (3M-1)N$, and the number of SBL iterations necessary for convergence, denoted by $\wp$. In the proposed approach, M, N, and G are the design choices available for a specified maximum value of Q. For the numerical experiments described in Section IV, it was observed that, on average, the number of iterations, $\wp$, required for the convergence of the algorithm when the SNR exceeds -10 dB is approximately 25.

A direct implementation of SBL requires matrix inversions in each iteration. However, recent results on SBL [61], [62] indicate that iterative techniques can converge to the solution without the explicit need for matrix inversions, and therefore can be used for further optimization. Thus, the proposed approach for DOA estimation can be considered a lightweight and complementary alternative to DL-based approaches.

Algorithm 1 Proposed SBL Algorithm for Azimuth DOA Estimation Using the Difference Co-Array of the CCUCA

Input: Q, G, M, N, R_1, R_2, λ, $\{\mathbf{x}_1(t)\}$, $\{\mathbf{x}_2(t)\}$ for $t = 1, 2, \ldots, T$
Output: $\widehat{\varphi}_1, \widehat{\varphi}_2, \ldots, \widehat{\varphi}_Q$
Parameters: $\Delta\varphi$, $\epsilon_{\min}$, *Max_Iterations*

$\widehat{\mathbf{R}}_{x_{12}} \leftarrow \mathbf{0}$
$t \leftarrow 0$, $\sigma^2 \leftarrow 1$, *Iteration* $\leftarrow 1$
$\boldsymbol{\gamma} = [\gamma_1, \gamma_2, \cdots, \gamma_G]^T \leftarrow [1, 1, \cdots, 1]^T$
$S_G \leftarrow \{1, 2, \ldots, G\}$
while $t \leq T-1$ **do**
  $\widehat{\mathbf{R}}_{x_{12}} \leftarrow \widehat{\mathbf{R}}_{x_{12}} + \frac{1}{T}\mathbf{x}_1(t)\mathbf{x}_2^H(t)$
  $t \leftarrow t+1$
end while
if $Q \geq \min(N, 3M-1)$ **then**
  $\widetilde{\mathbf{R}}_{x_{12}} \leftarrow \widehat{\mathbf{R}}_{x_{12}}$
else
  $\widehat{\mathbf{R}}_{x_{12}} = \mathbf{U}_{12}\boldsymbol{\Sigma}_{12}\mathbf{V}_{12}^H$
  $\widetilde{\mathbf{R}}_{x_{12}} \leftarrow \mathbf{U}_{12}(:, 1:Q)\boldsymbol{\Sigma}_{12}(1:Q, 1:Q)\mathbf{V}_{12}^H(:, 1:Q)$
end if
$\mathbf{z} \leftarrow \mathrm{vec}(\widetilde{\mathbf{R}}_{x_{12}})$
$L_z \leftarrow |\{\mathbf{z}\}| = (3M-1)N$
$\varphi \leftarrow 0$, $\boldsymbol{\Phi} \leftarrow \mathbf{0}$, $S_\varphi \leftarrow \emptyset$
while $\varphi \leq 2\pi$ **do**
  $\bar{\mathbf{a}}(\varphi) \leftarrow \mathbf{a}_1(\varphi) \otimes \mathbf{a}_2^*(\varphi)$
  $\boldsymbol{\Phi} \leftarrow [\boldsymbol{\Phi}; \bar{\mathbf{a}}(\varphi)]$
  $S_\varphi \leftarrow S_\varphi \cup \{\varphi\}$
  $\varphi \leftarrow \varphi + \Delta\varphi$
end while
while *Iteration* $\leq$ *Max_Iterations* **and** $\epsilon \geq \epsilon_{\min}$ **do**
  $\gamma_g^{old} \leftarrow \gamma_g$, $\forall g \in S_G$, *i.e.*, $\boldsymbol{\gamma}^{old} \leftarrow \boldsymbol{\gamma}$
  $\boldsymbol{\Sigma}_z \leftarrow \sigma^2\mathbf{I}_{L_z} + \boldsymbol{\Phi}\boldsymbol{\Gamma}\boldsymbol{\Phi}^H$
  for $g \in S_G$ **do**
    $\gamma_g \leftarrow \dfrac{\gamma_g^{old}\|\mathbf{z}^H\boldsymbol{\Sigma}_z^{-1}\boldsymbol{\Phi}(:, g)\|_2}{\sqrt{\boldsymbol{\Phi}(:, g)^H\boldsymbol{\Sigma}_z^{-1}\boldsymbol{\Phi}(:, g)}}$
  end for
  $\boldsymbol{\gamma} \leftarrow [\gamma_1, \ldots, \gamma_G]^T$, $\boldsymbol{\Gamma} \leftarrow \mathrm{diag}(\boldsymbol{\gamma})$
  $\Re_c \leftarrow \{g \in S_G \mid Q \text{ largest peaks in } \boldsymbol{\gamma}\}$
  $\boldsymbol{\Psi} \leftarrow \boldsymbol{\Phi}(:, \Re_c)$
  $\boldsymbol{\Psi}^{\dagger} \leftarrow (\boldsymbol{\Psi}^H\boldsymbol{\Psi})^{-1}\boldsymbol{\Psi}^H$
  $\sigma^2 \leftarrow \dfrac{1}{L_z - Q}\mathrm{Tr}\left\{(\mathbf{I}_{L_z} - \boldsymbol{\Psi}\boldsymbol{\Psi}^{\dagger})\mathbf{z}\mathbf{z}^H\right\}$
  Iteration $\leftarrow$ *Iteration* $+ 1$
  $\epsilon \leftarrow \dfrac{\|\boldsymbol{\gamma}^{old} - \boldsymbol{\gamma}\|_1}{\|\boldsymbol{\gamma}^{old}\|_1}$
end while
$\boldsymbol{\Sigma}_z \leftarrow \sigma^2\mathbf{I}_{L_z} + \boldsymbol{\Phi}\boldsymbol{\Gamma}\boldsymbol{\Phi}^H$
$\boldsymbol{\mu} \leftarrow \boldsymbol{\Gamma}\boldsymbol{\Phi}^H\boldsymbol{\Sigma}_{\mathbf{z}}^{-1}\mathbf{z}$ {MAP estimate of vector $\mathbf{z}$}
$\widehat{\varphi}_1, \widehat{\varphi}_2, \cdots, \widehat{\varphi}_Q$ correspond to $S_\varphi\left(\Re_c\right)$ {Values at indices of Q largest peaks in $\Re\mathrm{e}(\boldsymbol{\mu})$}

IV. PERFORMANCE EVALUATION USING NUMERICAL EXPERIMENTS

Numerical experiments are conducted to verify the performance of the proposed approach for azimuth DOA estimation using CCUCA and NSCA with SBL. In the first experiment, we consider the DOA estimation of 18 uncorrelated sources at azimuth angles, 5°, 15°, 27°, 37°, 48°, 60°, 90°, 100°, 116°, 128°, 151°, 160°, 170°, 200°, 240°, 259°, 311°, and 340° with unit power, SNR of 0 dB and number of snapshots,

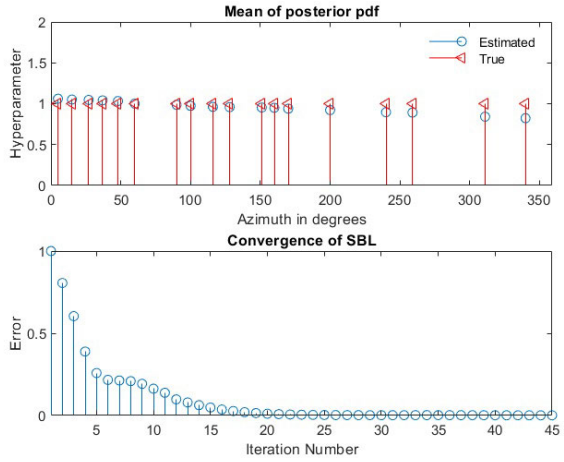

FIGURE 4. DOA estimation performance using the CCUCA with $M = 3$, $N = 7$: $R_1 = 4\lambda$, $R_2 = 5\lambda$, $Q = 18$, 0 dB SNR and 2000 snapshots.

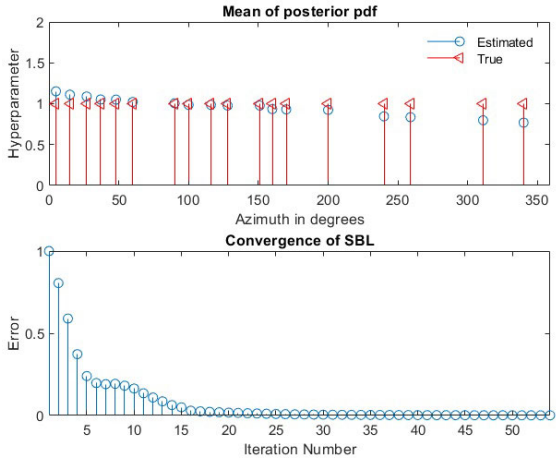

FIGURE 5. DOA estimation performance using the CCUCA with $M = 3$, $N = 7$: $R_1 = 4\lambda$, $R_2 = 4\lambda$, $Q = 18$, 0 dB SNR and 2000 snapshots.

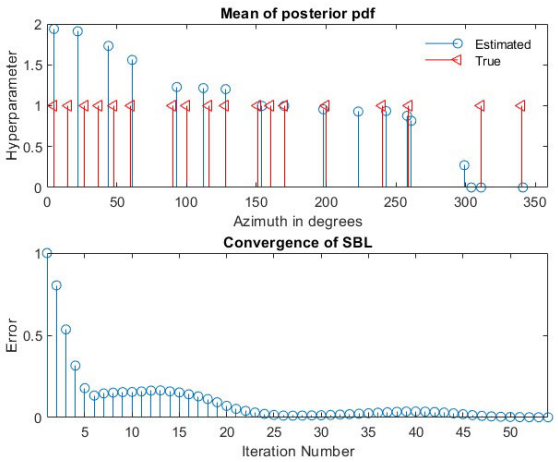

FIGURE 6. DOA estimation performance using the NSCA [48] with 15 antennas: radius = λ, $Q = 18$, 0 dB SNR and 2000 snapshots.

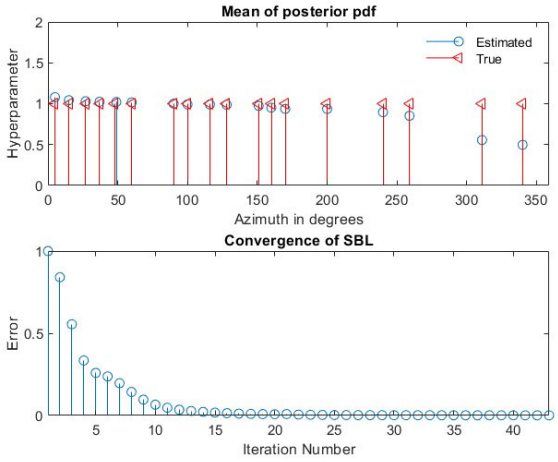

FIGURE 7. DOA estimation performance using the NSCA [48] with 15 antennas: radius = 4λ, $Q = 18$, 0 dB SNR and 2000 snapshots.

$T = 2000$. The azimuth grid has a step size of 1°. Performance is studied for two CCUCA geometries, *viz.*, $R_1 = 4\lambda$, $R_2 = 5\lambda$, $M = 3$, $N = 7$ and $R_1 = 4\lambda$, $R_2 = 4\lambda$, $M = 3$, $N = 7$, respectively.

Figure 4 and Fig. 5, respectively, show plots of the mean of the posterior pdf, whose indices represent the estimated azimuth DOAs, as well as the convergence of the SBL algorithm for the two CCUCA geometries. We observe that under the scenario of more sources than physical sensors and 0 dB SNR, the proposed approach correctly estimates the azimuth DOAs. This is not feasible when using subspace-based approaches with a physical sensor array because the maximum number of sources that can be handled is one less than the number of physical sensors. For NSCA, the performance for the same scenario is studied when the radius is equal to λ and 4λ, assuming the total number of antennas to be 15, which is the same as CCUCA for a fair comparison. In the NSCA, one antenna is located at the center, a dense circular sub-array, and a second circular sub-array, each having 7 antennas [48]. Figure 6 and Fig. 7 show the plots of the mean of the posterior pdf, as well as the convergence of the SBL algorithm for cases where the radius is equal to λ and 4λ, respectively. It can be seen that when the radius is equal to λ, the estimated DOAs are not accurate, whereas when the radius increases to 4λ, *i.e.* when the NSCA has a wider aperture, the performance improves.

In the second experiment, 200 Monte Carlo simulation runs are performed to study the statistical performance of the DOA estimation accuracy in terms of bias and RMS error, as a function of the SNR for different numbers of snapshots. The SNR ranges from -12 dB to 20 dB in steps of 4 dB. Figure 8 and Fig. 9, respectively, compare the bias and RMS accuracy plots for the CCUCA and NSCA geometries using 1000 snapshots. The number of uncorrelated sources assumed is $Q = 4$, with their true azimuth DOAs being 15°, 65°, 228°, and 347°, respectively. Each source is assumed to have unit power. The CCUCA geometries considered have the parameters $M = 3$, $N = 7$ and $R_1 = 4\lambda$, $R_2 = 5\lambda$ and

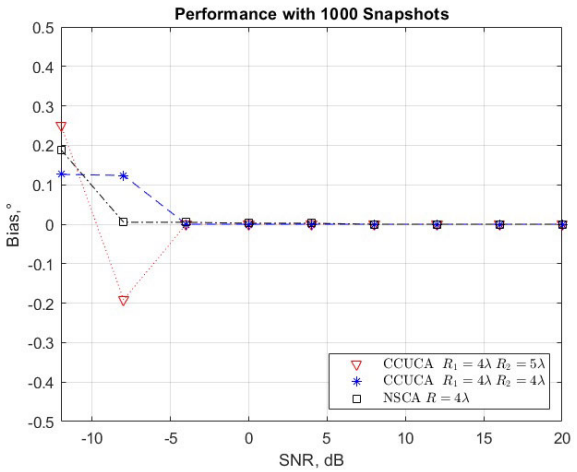

FIGURE 8. Bias of DOA estimation performance as a function of SNR with 1000 snapshots.

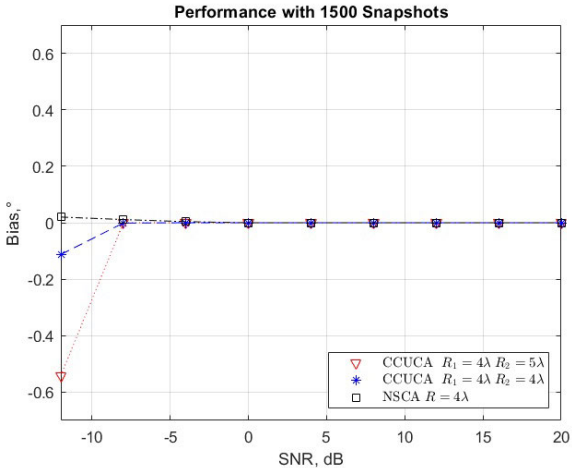

FIGURE 10. Bias of DOA estimation performance as a function of SNR with 1500 snapshots.

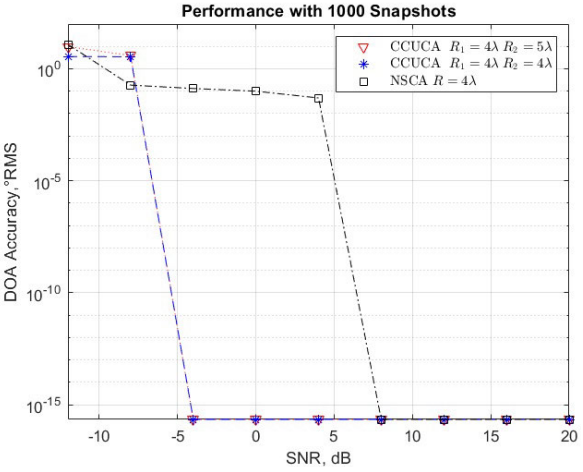

FIGURE 9. RMS accuracy of DOA estimation performance as a function of SNR with 1000 snapshots.

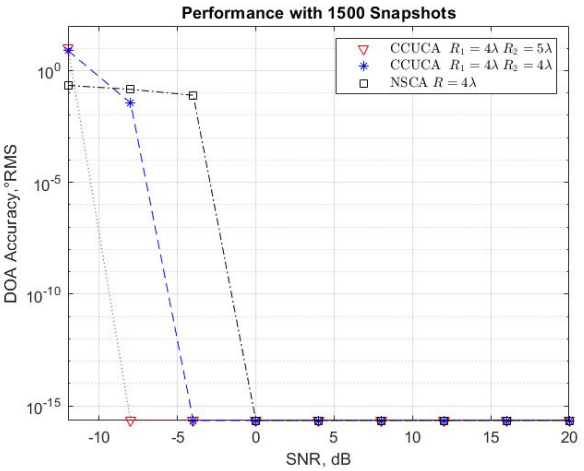

FIGURE 11. RMS accuracy of DOA estimation performance as a function of SNR with 1500 snapshots.

$M = 3$, $N = 7$ and $R_1 = 4\lambda$, $R_2 = 4\lambda$. The NSCA geometry [48] considered has a wide aperture with a radius of 4λ. Figure 10 to Fig. 13 present the performance study for the same source scenario and array geometries when the number of snapshots is 1500 and 2000, respectively. We showed that the performance of the NSCA improved as a result of a wider aperture. From Fig. 8 to Fig. 13, we can see that the accuracy of the DOA improves with the SNR, as well as the number of snapshots. Furthermore, as the SNR increases, both the bias and RMS $\rightarrow 0$ when the true DOAs are on the sampling grid. We therefore observe from the simulation results that the proposed CCUCA geometry not only provides improved performance but also overcomes most of the practical installation limitations of the NSCA on commonly used EW surveillance platforms *viz.*, the requirement for an antenna to be located at the center of the array, azimuth asymmetry in the array geometry, dense circular sub-array that increases mutual coupling, and difficulty to install the larger sized antennas when operating at higher frequencies.

V. DESIGN OF A NOVEL PASSIVE FREQUENCY-INDEPENDENT CCUCA SIMULATOR

Performance evaluation of any of the developed DOA estimation techniques using real system hardware should be carried out at an open area test site (OATS) before the field deployment of the system [3], [35]. Measurement campaigns are time-consuming, cumbersome, and expensive. Therefore, an antenna array simulator is required to evaluate the performance of the DOA estimation technique on a real-life hardware platform before moving to an OATS. An antenna array simulator generates controlled RF test signals of appropriate phases that would be received if the antenna array were receiving from the EM fields produced by a far-field source. The antenna array simulator could be either active or passive. Active simulator [63] is usually realized using user-programmable digital and mixed-signal electronics, whereas passive simulators are realized with RF delay lines or RF cable sets, which are fed by phase-coherent RF signals obtained by power division of

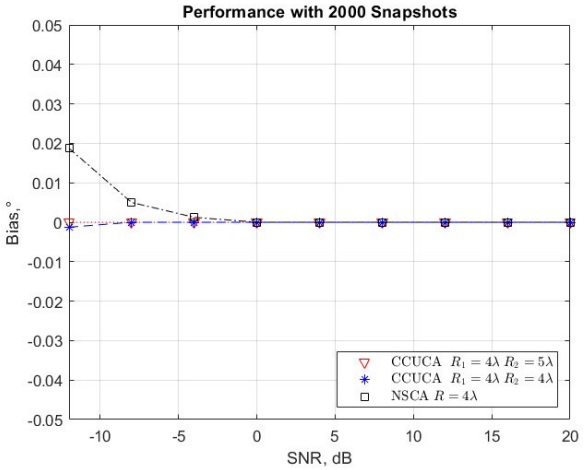

FIGURE 12. Bias of DOA estimation performance as a function of SNR with 2000 snapshots.

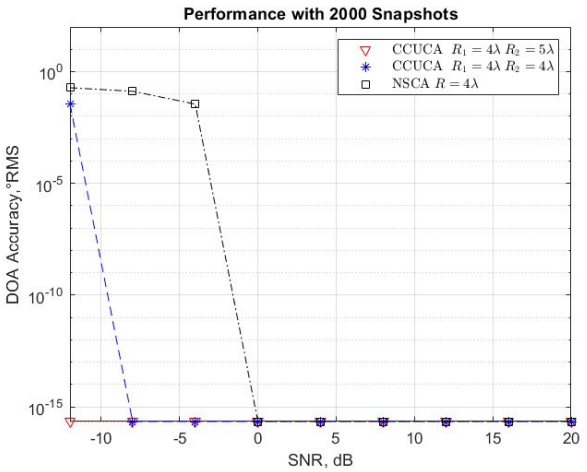

FIGURE 13. RMS accuracy of DOA estimation performance as a function of SNR with 2000 snapshots.

an RF signal generated by a test instrument such as an RF signal generator. Passive antenna array simulators, due to their inherent simplicity, are frequently used for laboratory testing of DOA estimation algorithms by injecting signals into the system realized using phase-coherent multichannel RF and Digital Signal Processing (DSP) hardware [3], [52].

We now design a novel passive frequency-independent CCUCA simulator. To the best of our knowledge, such a novel design that is frequency-independent is not reported in the literature. This simulator generates signals that would be received by the array from a fixed azimuth when illuminated by the EM wavefront from a single source. An interesting aspect of this simulator is that it is frequency-independent, and hence can be used for testing with any type of arbitrary signal waveform. In practical systems employing narrowband DOA estimation techniques, to cover a wide frequency band in applications like SM and EW, where there is no prior information available on the frequency and waveform of the far-field sources, the DOA estimation is performed by a phase-coherent frequency channel scanning hardware separately for each narrowband channel [3], [52]. Since DOA is the only parameter that cannot be camouflaged due to its dependency on the geo-location of the source, by fusing DOA information from multiple narrowband frequency channels obtained by processing, it becomes relatively easy to handle low probability of intercept (LPI) waveforms like direct sequence spread spectrum (DSSS), frequency hopping (FH), chirp, and burst.

Figure 14 shows the design of a passive frequency-independent CCUCA simulator that generates signals received from a fixed azimuth φ. The set $\{L_m\}$, $m \in S_1'$ represents the lengths of the RF delay lines for UCA 1. Similarly, the lengths of the RF delay lines for UCA 2 are denoted by the set $\{\widetilde{L}_n\}$, $n \in S_2''$. Together, these sets of RF delay lines along with the RF signal generator generate a signal with appropriate phase differences similar to what would exist when UCA 1 and UCA 2 receive signals from azimuth φ. We make the following assumptions for the design.

a. The dielectric constant for the RF delay lines used in the design is ϵ_r, which means that the speed of the EM wave inside the delay line is $\frac{C}{\sqrt{\epsilon_r}}$, with C, being the speed of an EM wave in free space.
b. The antennas are isotropic and there is no mutual coupling between any pair of antennas.
c. There is no multipath propagation. Only direct line of sight (LOS) propagation exists from a far-field source to the CCUCA.

The length of the RF delay lines can be calculated using (11) and (14). Without loss of generality, we assume that the first antenna of UCA 1 is located at angle $\nu_1' = (1-M)\,\alpha$ as the reference for all phase difference calculations. Therefore, the phase differences of the signals received at all other antennas of UCA 1, ξ_m, $m \in S_1'$, $m \neq 1$, and UCA 2, $\widetilde{\xi}_n$, $n \in S_2''$ with respect to the signal received at the reference antenna are obtained from (11) and (14), respectively, as,

$$\begin{aligned}\xi_m &= \psi_m'(\varphi) - \psi_1'(\varphi), \\ &= \frac{2\pi R_1}{\lambda}\left\{\cos\left(\nu_m' - \varphi\right) - \cos\left(\nu_1' - \varphi\right)\right\}, \end{aligned} \tag{64}$$

with, $m \in S_1'$, $m \neq 1$, and

$$\begin{aligned}\widetilde{\xi}_n &= \psi_n''(\varphi) - \psi_1'(\varphi), \\ &= \frac{2\pi}{\lambda}\left\{R_2\cos\left(\nu_n'' - \varphi\right) - R_1\cos\left(\nu_1' - \varphi\right)\right\}, \end{aligned} \tag{65}$$

with $n \in S_2''$.

However, the phase differences due to delay lines of length L_m, $m \in S_1'$, $m \neq 1$ and $\widetilde{L}_n$, $n \in S_2''$ respectively, with respect to the signal propagating through the delay line of length L_1, are given by,

$$\xi_m = \frac{2\pi\sqrt{\epsilon_r}}{\lambda}\left(L_1 - L_m\right), \; m \in S_1', \; m \neq 1, \tag{66}$$

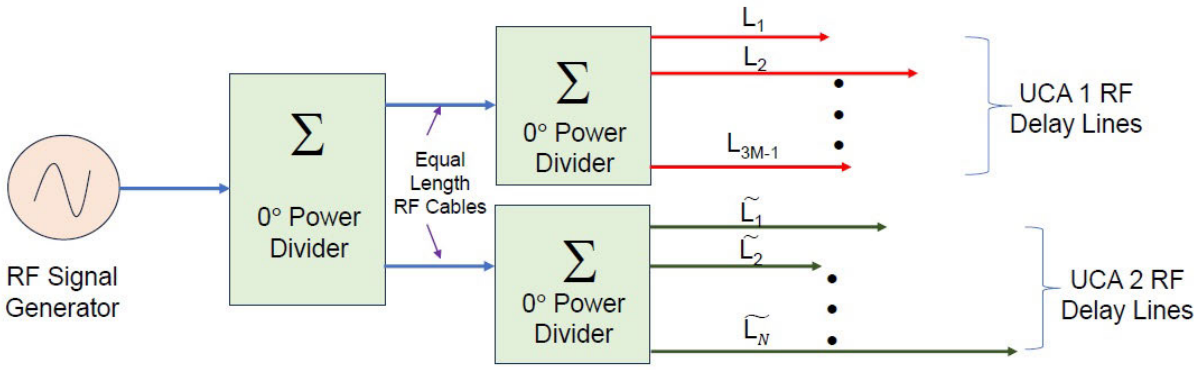

FIGURE 14. Passive frequency-independent CCUCA simulator.

and

$$\widetilde{\xi}_n = \frac{2\pi\sqrt{\epsilon_r}}{\lambda}\left(L_1 - \widetilde{L}_n\right),\ n \in \mathrm{S}_2''. \tag{67}$$

This follows from the fact that path differences manifest in the form of phase differences when the EM wave propagates in RF cables at a speed $\frac{C}{\sqrt{\epsilon_r}}$. Therefore, we can equate (64) with (66) and (65) with (67), and obtain the lengths of the RF delay lines of the CCUCA simulator as

$$L_m = L_1 - \frac{R_1}{\sqrt{\epsilon_r}}\left\{\cos\left(\nu_m' - \varphi\right) - \cos\left(\nu_1' - \varphi\right)\right\}, \tag{68}$$

with $m \in \mathrm{S}_1'$, $m \neq 1$, and

$$\widetilde{L}_n = L_1 - \frac{R_2}{\sqrt{\epsilon_r}}\left\{\cos\left(\nu_n'' - \varphi\right)\right\} - \frac{R_1}{\sqrt{\epsilon_r}}\left\{\cos\left(\nu_1' - \varphi\right)\right\}, \tag{69}$$

with $n \in \mathrm{S}_2''$. It can be observed from (68) and (69) that the length of the delay lines depends only on the azimuth DOA that is simulated, φ, for a given M and N. There is no dependence on the frequency, due to which this passive CCUCA simulator is frequency-independent. In practice, the length of the reference RF delay line L_1 is chosen to be a convenient length like 1 meter, and the lengths of all other RF delay lines are calculated using (68) and (69). However, it should be ensured that ϵ_r of all RF delay lines is the same. In practice, the realized lengths of the RF delay lines are accurate to finite precision, and minor variations owing to manufacturing tolerances cause negligible variations in the simulated azimuth DOA.

VI. CONCLUSION

We introduced a novel CCUCA geometry for azimuth DOA estimation that is suitable for applications in SM and EW, especially with respect to platform installation constraints, less mutual coupling, and complete coverage of azimuth in contrast to sparse linear arrays. We demonstrated that the difference co-array of the CCUCA has a larger aperture than the physical array with a higher number of dense virtual sensors, as a result of which the DOA estimation of a larger number of sources than the number of physical sensors is feasible. In addition, we proposed an SBL-based DOA estimation algorithm exploiting the difference co-array of CCUCA. Numerical experiments have been carried out to verify the performance of the SBL algorithm with the CCUCA and NSCA geometries. Our simulation results indicate that the performance of the NSCA has improved with increasing the radius of the array. We have also demonstrated that the proposed CCUCA geometry overcomes many of the practical installation limitations posed by the NSCA on commonly used EW surveillance platforms. We proposed a novel passive frequency-independent CCUCA simulator that can be used for laboratory testing of the proposed approach, thus avoiding field measurement campaigns that are time-consuming, cumbersome, and expensive. The proposed approach for exploiting the difference co-array data using SBL can be easily extended to other geometries.

APPENDIX
COMPUTATIONAL REQUIREMENTS FOR THE PROPOSED APPROACH

We discuss the computational requirements for implementing Algorithm 1. We assume that the dictionary matrix $\mathbf{\Phi}$ is precomputed and the fixed constants C_1 to C_9, introduced below account for the multiplications and additions (or subtractions) required for some basic operations that can be understood from the context. We first consider the case $Q \geq \min(N,\ 3M-1)$.

i. Calculating $\widehat{\mathbf{R}}_{x_{12}}$ using T snapshots requires $L_z T$ multiplications and T additions, where $L_z = (3M-1)N$.
ii. The number of multiplications and additions required to calculate $\mathbf{\Sigma_z}$ are $L_z G\,(L_z+1)$ and $L_z\,\{L_z\,(G-1)+1\}$, respectively.
iii. The $\boldsymbol{\gamma}$ update requires approximately, $L_z^3 + 3GL_z^2 + C_1 G$ multiplications and $L_z^3 + 3(L_z-1)G + C_2 G$ additions, where C_1, and C_2 are fixed constants.

iv. The number of subtractions necessary to determine the Q peaks in the vector $\boldsymbol{\gamma}$ is C_3G, where C_3 is a fixed constant.
v. The update of σ^2 requires approximately $L_z^3 + L_z^2(Q+1) + L_zQ^2 + 1$ multiplications and $L_z^3 + L_z^2(Q-1) + L_z(Q^2+2) - 1$ additions.
vi. The update of ϵ, requires approximately $G + C_4$ multiplications and $2G - 1 + C_5$ additions, where C_4, and C_5 are fixed constants.

Let $\wp$ denote the total number of iterations necessary for the convergence of SBL. Therefore, the total number of estimated multiplications, $\mathfrak{M}$, is given by

$$\mathfrak{M} = \wp\left\{GK_1 + 2L_z^3 + L_z^2K_2 + L_zQ^2 + C_4 + 1\right\}, \quad \text{(A-1)}$$

with,

$$K_1 = \left(4L_z^2 + L_z + C_1 + 1\right),$$
$$K_2 = (Q+1). \quad \text{(A-2)}$$

Similarly, the total number of estimated additions, $\mathfrak{A}$, is given by

$$\mathfrak{A} = \wp\left\{GK_3 + 2L_z^3 + L_z^2K_4 + L_zK_5 + C_5 - 1\right\}, \quad \text{(A-3)}$$

with,

$$K_3 = \left(L_z^2 + 3L_z + C_2 + C_3 + 1\right),$$
$$K_4 = (Q-2),$$
$$K_5 = \left(Q^2 + 3\right). \quad \text{(A-4)}$$

The case $Q < \min(N, 3M-1)$, requires computing the SVD of $\widetilde{\mathbf{R}}_{x_{12}}$ to obtain a rank-reduced approximation. In this case, $\mathfrak{M}$ given in (A-1) and $\mathfrak{A}$ given in (A-3) are respectively, increased approximately by, $C_6K_6Q^2 + C_7Q^3 + (3M-1)Q(N+1)$, and $C_8K_6Q^2 + C_9Q^3 + (3M-1)Q(N-1)$, with fixed constants C_6, C_7, C_8, C_9, and $K_6 = \max(N, 3M-1)$.

REFERENCES

[1] H. L. V. Trees, *Optimum Array Processing: Part-IV of Detection, Estimation, and Modulation Theory*. Hoboken, NJ, USA: Wiley, 2002, pp. 17–89.
[2] N. O'Donoughue, *Emitter Detection and Geolocation for Electronic Warfare*. Norwood, MA, USA: Artech House, 2020, pp. 85–182.
[3] E. Tuncer and B. Friedlander, *Classical and Modern Direction of Arrival Estimation*. Burlington, MA, USA: Academic, 2009, pp. 1–92.
[4] D. Vaccaro, *Electronic Warfare Receiving Systems*. Norwood, MA, USA: Artech House, 1993, pp. 221–259.
[5] H. Krim and M. Viberg, "Two decades of array signal processing research: The parametric approach," *IEEE Signal Process. Mag.*, vol. 13, no. 4, pp. 67–94, Jul. 1996.
[6] D. Malioutov, M. Cetin, and A. S. Willsky, "A sparse signal reconstruction perspective for source localization with sensor arrays," *IEEE Trans. Signal Process.*, vol. 53, no. 8, pp. 3010–3022, Aug. 2005.
[7] E. J. Candes and M. B. Wakin, "An introduction to compressive sampling," *IEEE Signal Process. Mag.*, vol. 25, no. 2, pp. 21–30, Mar. 2008.
[8] M. Elad, *Sparse and Redundant Representations: From Theory to Applications in Signal and Image Processing*, 1st ed., Cham, Switzerland: Springer, 2010, pp. 3–108.
[9] L. Stanković, E. Sejdić, S. Stanković, M. Daković, and I. Orović, "A tutorial on sparse signal reconstruction and its applications in signal processing," *Circuits, Syst., Signal Process.*, vol. 38, no. 3, pp. 1206–1263, Mar. 2019.
[10] E. Crespo Marques, N. Maciel, L. Naviner, H. Cai, and J. Yang, "A review of sparse recovery algorithms," *IEEE Access*, vol. 7, pp. 1300–1322, 2019.
[11] Z. Zhang, Y. Xu, J. Yang, X. Li, and D. Zhang, "A survey of sparse representation: Algorithms and applications," *IEEE Access*, vol. 3, pp. 490–530, 2015.
[12] P. Pal and P. P. Vaidyanathan, "Nested arrays: A novel approach to array processing with enhanced degrees of freedom," *IEEE Trans. Signal Process.*, vol. 58, no. 8, pp. 4167–4181, Aug. 2010.
[13] P. P. Vaidyanathan and P. Pal, "Sparse sensing with co-prime samplers and arrays," *IEEE Trans. Signal Process.*, vol. 59, no. 2, pp. 573–586, Feb. 2011.
[14] S. Qin, Y. D. Zhang, and M. G. Amin, "Generalized coprime array configurations for direction-of-arrival estimation," *IEEE Trans. Signal Process.*, vol. 63, no. 6, pp. 1377–1390, Mar. 2015.
[15] C.-L. Liu and P. P. Vaidyanathan, "Super nested arrays: Linear sparse arrays with reduced mutual coupling—Part I: Fundamentals," *IEEE Trans. Signal Process.*, vol. 64, no. 15, pp. 3997–4012, Aug. 2016.
[16] M. G. Amin, *Sparse Arrays for Radar, Sonar, and Communications*. Hoboken, NJ, USA: Wiley, 2023.
[17] P. Kulkarni and P. P. Vaidyanathan, "Non-integer arrays for array signal processing," *IEEE Trans. Signal Process.*, vol. 70, pp. 5457–5472, 2022.
[18] R. Schmidt, "Multiple emitter location and signal parameter estimation," *IEEE Trans. Antennas Propag.*, vol. AP-34, no. 3, pp. 276–280, Mar. 1986.
[19] R. Roy and T. Kailath, "ESPRIT-estimation of signal parameters via rotational invariance techniques," *IEEE Trans. Acoust., Speech, Signal Process.*, vol. 37, no. 7, pp. 984–995, Jul. 1989.
[20] Z. Zhang and B. D. Rao, "Sparse signal recovery with temporally correlated source vectors using sparse Bayesian learning," *IEEE J. Sel. Topics Signal Process.*, vol. 5, no. 5, pp. 912–926, Sep. 2011.
[21] C. F. Mecklenbriiuker, P. Gerstoft, and G. Leus, "Sparse Bayesian learning for DOA estimation of correlated sources," in *Proc. IEEE 10th Sensor Array Multichannel Signal Process. Workshop (SAM)*, Jul. 2018, pp. 533–537.
[22] A. Ishimaru, "Theory of unequally-spaced arrays," *IRE Trans. Antennas Propag.*, vol. 10, no. 6, pp. 691–702, Nov. 1962.
[23] R. T. Hoctor and S. A. Kassam, "The unifying role of the coarray in aperture synthesis for coherent and incoherent imaging," *Proc. IEEE*, vol. 78, no. 4, pp. 735–752, Apr. 1990.
[24] A. Moffet, "Minimum-redundancy linear arrays," *IEEE Trans. Antennas Propag.*, vol. AP-16, no. 2, pp. 172–175, Mar. 1968.
[25] P. P. Vaidyanathan and P. Pal, "Direct-MUSIC on sparse arrays," in *Proc. Int. Conf. Signal Process. Commun. (SPCOM)*, Jul. 2012, pp. 1–5.
[26] P. P. Vaidyanathan and P. Pal, "Why does direct-MUSIC on sparse-arrays work?" in *Proc. Asilomar Conf. Signals, Syst. Comput.*, Nov. 2013, pp. 2007–2011.
[27] P. Pal and P. P. Vaidyanathan, "Coprime sampling and the music algorithm," in *Proc. Digit. Signal Process. Signal Process. Educ. Meeting (DSP/SPE)*, Jan. 2011, pp. 289–294.
[28] Y. D. Zhang, M. G. Amin, and B. Himed, "Sparsity-based DOA estimation using co-prime arrays," in *Proc. IEEE Int. Conf. Acoust., Speech Signal Process.*, May 2013, pp. 3967–3971.
[29] C. Stöeckle, J. Munir, A. Mezghani, and J. A. Nossek, "DoA estimation performance and computational complexity of subspace- and compressed sensing-based methods," in *Proc. 19th Int. ITG Workshop Smart Antennas (WSA)*, Mar. 2015, pp. 1–6.
[30] M. Tipping, "Sparse Bayesian learning and relevance vector machine," *J. Mach. Learn. Res.*, vol. 1, pp. 211–244, Jan. 2001.
[31] P. Gerstoft, C. F. Mecklenbräuker, A. Xenaki, and S. Nannuru, "Multi-snapshot sparse Bayesian learning for DOA," *IEEE Signal Process. Lett.*, vol. 23, no. 10, pp. 1469–1473, Oct. 2016.
[32] S. Nannuru, P. Gerstoft, A. Koochakzadeh, and P. Pal, "Sparse Bayesian learning for DOA estimation using co-prime and nested arrays," in *Proc. IEEE 10th Sensor Array Multichannel Signal Process. Workshop (SAM)*, Jul. 2018, pp. 519–523.
[33] M. Carlin, P. Rocca, G. Oliveri, F. Viani, and A. Massa, "Directions-of-arrival estimation through Bayesian compressive sensing strategies," *IEEE Trans. Antennas Propag.*, vol. 61, no. 7, pp. 3828–3838, Jul. 2013.

[34] S. Qin, Y. D. Zhang, and M. G. Amin, "Improved two-dimensional DOA estimation using parallel coprime arrays," *Signal Process.*, vol. 172, Jul. 2020, Art. no. 107428.
[35] R. L. Kellog, E. E. Mack, and C. D. Crews, "Direction finding antennas and systems," in *Antenna Engineering Handbook*. New York, NY, USA: McGraw-Hill, 2007, ch. 4.
[36] A. M. Elbir, "V-shaped sparse arrays for 2-D DOA estimation," *Circuits, Syst., Signal Process.*, vol. 38, no. 6, pp. 2792–2809, Jun. 2019, doi: 10.1007/s00034-018-0991-5.
[37] A. M. Elbir, "L-shaped coprime array structures for DOA estimation," *Multidimensional Syst. Signal Process.*, vol. 31, no. 1, pp. 205–219, Jan. 2020.
[38] S. Wang, W. Chen, and B. Ai, "Off-grid DOA estimation on uniform plane array based on structured sparse Bayesian learning," in *Proc. IEEE/CIC Int. Conf. Commun. China (ICCC)*, Aug. 2023, pp. 1–6.
[39] A. M. Elbir, "DeepMUSIC: Multiple signal classification via deep learning," *IEEE Sensors Lett.*, vol. 4, no. 4, pp. 1–4, Apr. 2020.
[40] G. K. Papageorgiou and M. Sellathurai, "Direction-of-arrival estimation in the low-SNR regime via a denoising autoencoder," in *Proc. IEEE 21st Int. Workshop Signal Process. Adv. Wireless Commun. (SPAWC)*, May 2020, pp. 1–5.
[41] G. K. Papageorgiou, M. Sellathurai, and Y. C. Eldar, "Deep networks for direction-of-arrival estimation in low SNR," *IEEE Trans. Signal Process.*, vol. 69, pp. 3714–3729, 2021.
[42] H. A. Kassir, N. V. Kantartzis, P. I. Lazaridis, P. Sarigiannidis, S. K. Goudos, C. G. Christodoulou, and Z. D. Zaharis, "Improving DOA estimation via an optimal deep residual neural network classifier on uniform linear arrays," *IEEE Open J. Antennas Propag.*, vol. 5, pp. 460–473, 2024.
[43] C. M. Mylonakis, P. Velanas, and Z. D. Zaharis, "On the implementation of temporal fusion transformers for target recognition and tracking," in *Proc. IEEE Wireless Commun. Netw. Conf. (WCNC)*, Mar. 2025, pp. 1–6.
[44] H. A. Kassir, C. S. Antonopoulos, and Z. D. Zaharis, "TBF-CM: A transformer-based beamforming framework leveraging correlation matrix information," *IEEE Trans. Antennas Propag.*, vol. 73, no. 10, pp. 7862–7871, Oct. 2025.
[45] Y. Xie, A. Liu, X. Lu, and D. Chong, "Hybrid multi-class token vision transformer convolutional network for DOA estimation," *IEEE Signal Process. Lett.*, vol. 32, pp. 2279–2283, 2025.
[46] T. Basikolo, K. Ichige, and H. Arai, "Underdetermined DOA estimation for uniform circular array based on sparse signal reconstruction," in *Proc. Int. Symp. Antennas Propag. (ISAP)*, Oct. 2016, pp. 1012–1013.
[47] T. Basikolo, K. Ichige, and H. Arai, "Direction of arrival estimation for quasi-stationary signals using nested circular array," in *Proc. 4th Int. Workshop Compressed Sens. Theory Appl. Radar, Sonar Remote Sens. (CoSeRa)*, Sep. 2016, pp. 193–196.
[48] T. Basikolo, K. Ichige, and H. Arai, "Nested circular array and its concentric extension for underdetermined direction of arrival estimation," *IEICE Trans. Commun.*, vol. 101, no. 4, pp. 1076–1084, 2018.
[49] S. Wandale, T. Basikolo, and K. Ichige, "Super nested sparse circular array for high resolution DOA estimation and its wideband extension," in *Proc. Int. Radar Conf. (RADAR)*, Sep. 2019, pp. 1–4.
[50] D. P. Wipf and B. D. Rao, "Sparse Bayesian learning for basis selection," *IEEE Trans. Signal Process.*, vol. 52, no. 8, pp. 2153–2164, Aug. 2004.
[51] S. Pandav and P. Ubaidulla, "Two-dimensional DOA estimation with modified parallel coprime linear sub-arrays," in *Proc. 10th Int. Conf. Wireless Commun. Signal Process. (WCSP)*, Oct. 2018, pp. 1–5.
[52] S. Chaudhary and A. Samant, "Characterization and calibration techniques for multi-channel phase-coherent systems," *IEEE Instrum. Meas. Mag.*, vol. 19, no. 4, pp. 44–50, Aug. 2016.
[53] U. Madhow, *Fundamentals of Digital Communication*. Cambridge, U.K.: Cambridge Univ. Press, 2008, pp. 7–41.
[54] G. H. Golub and C. F. V. Loan, *Matrix Computations*, 4th ed., Baltimore, MD, USA: Johns Hopkins University Press, 2013, ch. 2, pp. 76–81.
[55] D. L. Donoho, "Compressed sensing," *IEEE Trans. Inf. Theory*, vol. 52, no. 4, pp. 1289–1306, Apr. 2006.
[56] A. Xenaki and P. Gerstoft, "Grid-free compressive beamforming," *J. Acoust. Soc. Amer.*, vol. 137, no. 4, pp. 1923–1935, Apr. 2015, doi: 10.1121/1.4916269.
[57] K. L. B. Harry, L. Van Trees, and Z. Tian, *Detection, Estimation, and Modulation Theory, Part-1: Detection, Estimation, and Filtering Theory*. Hoboken, NJ, USA: Wiley, 2013, pp. 487–495.
[58] U. Spagnolini, *Statistical Signal Processing in Engineering*. Hoboken, NJ, USA: Wiley, 2018, pp. 4–5.
[59] J. R. Magnus and H. Neudecker, *Matrix Differential Calculus With Applications in Statistics and Econometrics*, 3rd ed., Hoboken, NJ, USA: Wiley, 2019, p. 165.
[60] A. G. Jaffer, "Maximum likelihood direction finding of stochastic sources: A separable solution," in *Proc. Int. Conf. Acoust., Speech, Signal Process. (ICASSP)*, 1988, pp. 2893–2896.
[61] H. Duan, L. Yang, J. Fang, and H. Li, "Fast inverse-free sparse Bayesian learning via relaxed evidence lower bound maximization," *IEEE Signal Process. Lett.*, vol. 24, no. 6, pp. 774–778, Jun. 2017.
[62] A. Sant, M. Leinonen, and B. D. Rao, "Block-sparse signal recovery via general total variation regularized sparse Bayesian learning," *IEEE Trans. Signal Process.*, vol. 70, pp. 1056–1071, 2022.
[63] N. Ergezer and H. Nayir, "A low cost HF direction finding antenna array simulator for verification of HF-DF receivers," in *Proc. IEEE AUTOTEST*, Sep. 2014, pp. 293–297.

SANJAY PANDAV received the B.E. degree in electronics and communication engineering from the University College of Engineering, Osmania University, Hyderabad, in 1997, and the M.Tech. degree in communication engineering from IIT Bombay, Mumbai, in 2000. He is currently pursuing the Ph.D. degree in electronics and communication engineering with the Signal Processing and Communications Research Center (SPCRC), IIIT Hyderabad. From 1997 to 1998, he was a Member Technical with D. E. Shaw India Software Pvt. Ltd., Hyderabad. Since 2000, he has been with DLRL, DRDO, Hyderabad, focusing on Communication Electronic Warfare. He has designed and implemented Direction Finding Systems that have been deployed in operational environments.

P. UBAIDULLA (Senior Member, IEEE) received the B.Tech. degree in electronics and communication engineering from the National Institute of Technology Calicut (NIT), Calicut, in 1997, the M.E. degree in communication engineering from NIT, Tiruchirappalli, in 2001, and the Ph.D. degree in electrical communication engineering from Indian Institute of Science (IISc), Bengaluru, India, in 2011. He was a member of the Research Staff with the Central Research Laboratory, Bharat Electronics Ltd. (BEL), prior to his doctoral studies. From 2011 to 2013, he was a Postdoctoral Fellow with the Computer, Electrical and Mathematical Sciences and Engineering (CEMSE) Division, King Abdullah University of Science and Technology (KAUST), Saudi Arabia. From 2013 to 2023, he was an Assistant Professor with the Signal Processing and Communications Research Center (SPCRC), International Institute of Information Technology (IIIT) Hyderabad. He is currently an Independent Researcher. His research interests include the broad area of wireless communications, with a current focus on the application of deep learning in wireless communications, integrated sensing and communication (ISAC), 6G networks, and flexible position antennas. He was a recipient of the Best Paper Award at the 10th International Symposium on Wireless Personal Multimedia Communications (WPMC 2007) and the Visvesvaraya Young Faculty Research Fellowship from the Ministry of Electronics and Information Technology, Government of India.